

REGULAR PAPER

Sliding mode corrector for jet UAV control

X. Wang 

Aerospace Engineering, University of Nottingham, Nottingham, United Kingdom
Email: wangxinhua04@gmail.com

Received: 3 January 2023; **Revised:** 18 March 2023; **Accepted:** 20 March 2023

Keywords: Sliding mode corrector; position sensing; jet UAV; system uncertainties

Abstract

A sliding mode corrector is presented for disturbance rejection in position sensing using relatively accurate velocity measurement. The corrector design is based on a robust second-order sliding mode (2-sliding mode), which makes the fusion of position and velocity on a sliding surface to reject disturbance. Even when the frequency bands of disturbance and actual position signal overlap, or large-magnitude disturbance exists, the corrector can still provide the accurate and smoothed estimate of position. The proposed corrector is applied to a jet UAV navigation and control. In the unmanned aerial vehicle (UAV) system, the disturbances exist in position and attitude measurements, and the uncertainties exist in the system dynamics. For the UAV trajectory tracking control, the system model is constructed in the earth-fixed frame, and the constructed model is fit for observer design to estimate system uncertainties. The control laws are designed according to the correction of position and attitude by the correctors and the estimation of system uncertainties by an existing observer. Finally, the flight experiment demonstrates the effectiveness of the proposed method.

Nomenclature

$p_m(t)$	position measurement
$p_0(t)$	actual position
$d_1(t)$	disturbance in position measurement
L_1	upper-bound of position disturbance
$v_m(t)$	velocity measurement
$v_0(t)$	actual velocity
$d_2(t)$	disturbance in velocity measurement
L_2	upper-bound of velocity disturbance
ε	upper-bound of sensor accuracy ratio
e_1	sliding variable
e_2	sliding variable
k_1	corrector parametre
k_2	corrector parametre
k_3	corrector parametre
ω_1	position disturbance frequency
$\rho(\omega_1)$	disturbance rejection ratio
x	position in earth-fixed frame x-direction
y	position in earth-fixed frame y-direction
z	position in earth-fixed frame z-direction
ϕ	roll angle
θ	pitch angle
ψ	yaw angle
α	angle-of-attack
β	sideslip angle

U	linear velocity in body frame axis x_b
V	linear velocity in body frame axis y_b
W	linear velocity in body frame axis z_b
Γ	the earth-fixed frame
Λ	the body frame
m	UAV mass
g	gravity acceleration
Ω_Λ	angular rate vector
Ω_Γ	Euler angle derivative vector
F	total external force
F_{jet}	thrust by jet engine
F_w	aerodynamic forces on the fixed wing
F_f	aerodynamic forces on the fuselage
F_r	forces created by the rudders
F_e	forces created by the elevators
F_d	uncertainties and external disturbances
τ	total moment
τ_w	moments created by the fixed wings
τ_r	moments created by the rudders
τ_e	moments created by the elevators
τ_d	moments due to the uncertainties and external disturbances
ρ	air density
S_w	area of the half wing
C_{L0}	fixed wing lift coefficient when the angle-of-attack α equals zero
$C_{L\alpha}$	fixed wing lift coefficient due to the angle-of-attack α
δ_i	fixed wing aileron deflection
$C_{L\delta_i}$	lift coefficient due to the aileron deflection δ_i
C_{D0}	fixed wing drag coefficient when $\alpha = \delta_i = 0$
A_w	aspect ratio of the fixed wing
e_w	value of the Oswald's efficiency factor
τ_{wa}	fixed wing aerodynamic moment
τ_{wc}	fixed wing control torque
S_f	fuselage equivalent cross-sectional area
L_f	lift force generated by the fuselage
D_f	drag force generated by the fuselage
C_{lf}	fuselage lift coefficient
C_{df}	fuselage drag coefficient
C_{df0}	fuselage constant in the coefficient of drag force
S_e	area of the elevator
δ_e	elevator deflection
$C_{le\alpha}$	elevator lift coefficient due to the angle-of-attack α and the deflection δ_e
C_{de0}	drag coefficient when $\alpha + \delta_e = 0$
A_e	aspect ratio of the elevator
e_e	the Oswald's efficiency factor
τ_{ea}	elevator aerodynamic moment
τ_{ec}	elevator control torque
S_r	area of the rudders
$C_{lr\beta}$	rudder lift coefficient due to the sideslip angle β
δ_r	rudder deflection
$C_{lr\delta_r}$	rudder lift coefficient due to the deflection δ_r
C_{dr0}	rudder drag coefficient when $\beta = \delta_r = 0$
A_r	aspect ratio of the rudder
e_r	rudder Oswald's efficiency factor
τ_{ra}	rudder aerodynamic moment
τ_{rc}	rudder control torque

Δ_x	uncertainty in x-direction
Δ_y	uncertainty in y-direction
Δ_z	uncertainty in z-direction
Δ_ϕ	uncertainty in roll
Δ_θ	uncertainty in pitch
Δ_ψ	uncertainty in yaw
y_{*1}	measurement for position/angle
y_{*2}	measurement for velocity/angular velocity
x_d	reference position in x-direction
y_d	reference position in y-direction
z_d	reference position in z-direction
ϕ_d	desired roll angle
θ_d	desired pitch angle
ψ_d	desired yaw angle
λ_{*1}	parametre of extended observer
λ_{*2}	parametre of extended observer
α_*	parametre of extended observer
k_{p1}	controller parametre in position dynamics
k_{p2}	controller parametre in position dynamics
k_{a1}	controller parametre in attitude dynamics
k_{a2}	controller parametre in attitude dynamics

1.0 Introduction

This paper considers correction of stochastic disturbance in position sensing and application to jet UAV navigation and control. This interest was motivated by the enormous civil and military applications of such fixed wing UAVs. It is one of the most attractive research focuses because the dynamical system of a jet UAV has many prominent features including powerful thrust provision, payload augmentation, high-speed flight and a high manoeuvrability [1–3]. UAV large-range flight needs information of global position, attitude and dynamic model, also flying velocity and angular velocity are necessary. However, in many cases, disturbances exist in position and attitude sensing, and uncertainties are inevitable in system modelling. These bring challenge for control.

In flight control systems, rational desired attitude is important for safe flight, and the determination of desired attitude needs the information of actual position and attitude [4]. However, disturbances in position and attitude sensing render the incorrect desired attitude, and the unwanted control command is generated. Constant sensing disturbance can be overcome through initial calibration. Comparing to constant sensing disturbance, time-varying position disturbance is more likely to render a serious mismatch between desired attitude and actual position, and it causes dangerous flight. Furthermore, the frequency bands of disturbance and actual position signal may overlap, and disturbance cannot be separated from actual position signal using the usual low-pass filters.

GPS (global positioning system) can provide global position information with accuracy of several metres or even tens of metres [5, 6]. Adverse environmental influences may contaminate GPS signals [6], and the position accuracy may become worse. Velocity is also important for UAV navigation and control. GPS can measure device velocity with two different accuracies: (1) large-error velocity by the difference method with accuracy of a metre per second due to position accuracy and noise effect; (2) accurate velocity by Doppler shift measurement with accuracy of a few centimetres, or even the accuracy approaching 5mm/s is possible [7, 8]. Alternatively, accurate velocity of device can be measured by a Doppler radar sensor with accuracy of a few centimetres [9]. Hence, measuring Doppler shift is a preferred way to get velocity. Except for sensing, velocity can be estimated from position using the observers or differentiators [10, 11]. However, relatively accurate measurement of position is required.

INS (inertial navigation system) can estimate position and velocity through integrations from acceleration measurement. However, measurement error or non-zero mean noise in acceleration through integrations cause velocity and position to drift over time. The observer-based INS methods were used to estimate unknown variables in navigation [12, 13]. However, position signals are limited to be local, but not global. For attitude information, an IMU (inertial measurement unit) can determine attitude angle from accurate angular velocity through integration, but angle drift happens. Meanwhile, the outputs of the accelerometers and the magnetometer in IMU can determine the large-error pitch, roll and yaw angles [14].

Uncertainties in UAV flight dynamics include: aerodynamic disturbance, unmodelled dynamics and parametric uncertainties. These uncertainties bring challenges for control system design. The uncertainty in a system can be estimated by an extended state observer [15, 16]. However, accurate position measurement is required as the input of observer. Even velocity can be used for estimation, disturbance in position cannot still be corrected. For a jet UAV flight control system, an integral-uncertainty observer was designed to estimate the attitude angles and attitude dynamic uncertainty, and an augmented observer was used to estimate the flying velocity and position dynamic uncertainty [17]. However, drift may happen for long-time flight due to effect of disturbance and actuator vibrations on the IMU. Meanwhile, the augmented observer can only reduce high-frequency noise, low- or mid-frequency disturbances still exist.

In order to reduce disturbances in position and attitude, the popular methods of GPS/INS based on KF (Kalman filter) or EKF (extended Kalman filter) are used for signal fusion to overcome the limits of individual measurements based on optimisation of a recursive least mean square error [18–21]. Thus, measurement accuracy is improved. For KF or EKF, the relatively accurate system models are needed. Furthermore, the uncertainty in noise statistics limits the performance. In addition, for EKF, system model linearisation may cause filtering divergence, and the derivation of the Jacobian matrices are non-trivial. A finite-time-convergent signal corrector was designed for position correction in a quadrotor UAV control system [22]. The signal corrector is complex, and the finite-time convergence cannot be implemented in engineering practice. Furthermore, the parameters' selection is sensitive to the estimate performance.

In this paper, a corrector based on robust 2-sliding mode is presented to correct position disturbance using relatively accurate velocity measurement. The 2-sliding mode can reduce the estimate errors of corrector and make the fusion of position and velocity on a linear sliding surface. Position disturbance is reduced further on the sliding surface. Not only the corrector can reject high-frequency noise, but also the low- and mid-frequency disturbances are reduced largely. Therefore, the corrector can reject low/mid/high frequency disturbances, and it is unrelated to the types of actual position signals. Due to the existence of linear sliding surface in the 2-sliding mode, the estimate outputs from the corrector are accurate and smoothed.

The contributions of the proposed corrector include: (1) the corrector can reject position disturbance in low/mid/high frequency bands; (2) due to the continuity of 2-sliding mode, the estimate outputs from the corrector are smoothed and accurate, and they can be used directly for control without any additional filters; (3) due to the robust sliding mode, the corrector parameters are highly inclusive to change of disturbance and signal; (4) because only switch logic and linear functions are used in the corrector, the corrector can be implemented easily in the current hardware of computational environments.

The proposed corrector is applied to navigation and control of a jet UAV. In the UAV flight test, the following adverse conditions are considered: disturbances in the measurements of GPS position and IMU attitude angles, and uncertainties in the UAV flight dynamics. For the UAV trajectory tracking control, the UAV system model is constructed in the earth-fixed frame [23]. Furthermore, the model is fit for observer design to estimate the system uncertainties. The correctors are adopted to correct the disturbances in GPS position and IMU attitude angles. In addition, an existing extended state observer [24] is used to estimate the uncertainties in the UAV flight dynamics. The performance of corrector is compared to the KF-based signal fusion methods [21, 25]. Moreover, based on the correction and estimation, the desired attitude is determined, and the control laws are designed to drive the UAV to achieve the flight mission.

2.0 Problem description

The problem considered in this paper is to reject disturbance in position and attitude sensing.

2.1 Position and velocity sensing

GPS provides position of a device, and accurate velocity can be determined by GPS with Doppler shift measurement or by a Doppler radar sensor.

Define the position measurement: $p_m(t) = p_0(t) + d_1(t)$, where, $p_0(t)$ is the actual position; $d_1(t)$ is the disturbance in position measurement, and $\sup_{t \in [0, \infty)} |d_1(t)| \leq L_1 < \infty$.

Define the velocity measurement: $v_m(t) = v_0(t) + d_2(t)$, where, $v_0(t)$ is the actual velocity; $d_2(t)$ is the disturbance in velocity measurement, and $\sup_{t \in [0, \infty)} |d_2(t)| \leq L_2 < \infty$.

Remark 2.1: The accuracy L_1 of GPS position sensing is usually a metre, a few metres or even tens of metres. Doppler shift measurement enables velocity accuracy L_2 of a few centimetres per second, even the accuracy approaching 5mm/s (i.e. 0.005m/s) is possible [8]. Therefore, $L_2 \ll 1$ holds. When using the consistent unit standard, we can get $L_2 \ll L_1$, i.e. the sensor accuracy ratio $\frac{L_2}{L_1} \ll 1$.

Furthermore, due to the reliability of Doppler measurement, velocity accuracy usually remains unchanged. However, the position accuracy may become worse because of different environmental influences, i.e. L_1 may increase. Therefore, there exists a small constant $\varepsilon > 0$, i.e. the upper-bound of sensor accuracy ratio, such that the sensor accuracy inequality $\max \left\{ \frac{L_2}{L_1} \right\} \leq \varepsilon \ll 1$ holds.

2.2 Attitude sensing

The gyroscopes in IMU provide the relatively accurate angular velocities, e.g. their accuracy is about $L_2 = 10^\circ/\text{hr} = 0.003^\circ/\text{s}$. The accuracy of attitude angles from IMU is relatively large, e.g. about $L_1 = 1.0^\circ$. Therefore, $\frac{L_2}{L_1} = \frac{0.003}{1} = 0.003 \ll 1$, and we can select an upper-bound of sensor accuracy ratio $0.003 \leq \varepsilon = 0.003 \ll 1$ to satisfy $\max \left\{ \frac{L_2}{L_1} \right\} \leq \varepsilon \ll 1$.

2.3 Effect of sensing disturbance on safe flight

Sensing disturbance has a serious impact on safe flight. Disturbance in position sensing may generate incorrect desired attitude angles, and they are mismatched to actual position trajectory. Therefore, the determined attitude is unwanted, and it may be dangerous.

In addition, in position measurement, the frequency bands of actual position $p_0(t)$ and sensing disturbance $d_1(t)$ may have intersections: the disturbance $d_1(t)$ may be in low-, mid- or high-frequency bands. It is impossible for the usual filters to separate $d_1(t)$ from the actual position signal $p_0(t)$.

Questions: How to reject disturbance $d_1(t)$ in position measurement $p_m(t)$ using the relatively accurate velocity $v_m(t)$? Also, how to reject the disturbance in angle measurement using the relatively accurate angular velocity?

3.0 Preliminary, corollary and notation

3.1 Preliminary

The related background is presented here.

Lemma 3.1 (sliding mode with prescribed convergence law) [26, 27]: The following system is considered:

$$\begin{aligned} \dot{e}_1 &= e_2 \\ \dot{e}_2 &= \varphi(t) + \gamma(t)\dot{u} \end{aligned} \tag{1}$$

where, e_1 and e_2 are the states; u is the controller, and \dot{u} in the system; $|\varphi(t)| \leq \Phi$, $0 < \Gamma_m \leq \gamma(t) \leq \Gamma_M$, $\Phi > 0$. A 2-sliding control algorithm is as follows:

$$\dot{u} = \begin{cases} -u, & \text{if } |u| > 1; \\ -V_M \text{sign}[e_2 + g(e_1)], & \text{if } |u| \leq 1 \end{cases} \quad (2)$$

where, $g(e_1)$ is smooth everywhere except on $e_1 = 0$, for example, $g(e_1) = k_1 |e_1|^\alpha \text{sign}(e_1)$, $\alpha \in [0.5, 1)$; $V_M > \frac{\Phi + \sup[g'(e_1)g(e_1)]}{\Gamma_m}$. Then, we get the finite-time convergence law $\dot{e}_1 = -g(e_1)$ (i.e. sliding surface $e_2 + g(e_1) = 0$), and there exists a finite time $t_s > 0$, for $t \geq t_s$, such that

$$e_1 = 0 \text{ and } e_2 = 0 \quad (3)$$

Remark 3.1: For system (1), when we select $\varphi(t) = 0$ and $\gamma(t) = 1$, it becomes

$$\begin{aligned} \dot{e}_1 &= e_2 \\ \dot{e}_2 &= \dot{u} \end{aligned} \quad (4)$$

Then, the 2-sliding control algorithm (2) is expressed by

$$\dot{u} = \dot{e}_2 = \begin{cases} -e_2, & \text{if } |e_2| > 1; \\ -V_M \text{sign}[e_2 + g(e_1)], & \text{if } |e_2| \leq 1 \end{cases} \quad (5)$$

3.2 Corollary on 2-sliding mode system

Combining the system (4) and the 2-sliding control algorithm (5), we get the following corollary on a 2-sliding mode with prescribed convergence law.

Corollary 3.1 (sliding mode with prescribed finite-time convergence law): A 2-sliding mode system is as follows:

$$\begin{aligned} \dot{e}_1 &= e_2 \\ \dot{e}_2 &= \begin{cases} -e_2, & \text{if } |e_2| > 1; \\ -V_M \cdot \text{sign}[e_2 + g(e_1)], & \text{if } |e_2| \leq 1 \end{cases} \end{aligned} \quad (6)$$

where, e_1 and e_2 are the sliding variables; $g(e_1)$ is smooth everywhere except on $e_1 = 0$, for example, $g(e_1) = k_1 |e_1|^\alpha \text{sign}(e_1)$, $\alpha \in [0.5, 1)$; $V_M > \sup[g'(e_1)g(e_1)]$. Then, we get the finite-time convergence law $\dot{e}_1 = -g(e_1)$ (i.e. sliding surface $e_2 + g(e_1) = 0$), and there exists a finite time $t_s > 0$, for $t \geq t_s$, such that

$$e_1 = 0 \text{ and } e_2 = 0 \quad (7)$$

Remark 3.2: For system (6), the parametre selection condition $V_M > \sup[g'(e_1)g(e_1)]$ is too strict. In order to relax the parametre selection conditions, we can use a linear convergence law $\dot{e}_1 = -k_1 e_1$ for the nonlinear $\dot{e}_1 = -g(e_1)$, and only $V_M > k_1 > 0$ will be required. In the following section, we will give a theorem on 2-sliding mode system with linear convergence law to be exponentially stable.

3.3 Notation

“ $a(\omega) : b_1 \rightarrow b_2$ as $\omega : c_1 \rightarrow c_2$ ” means that function $a(\omega)$ varies monotonically increasing or decreasing from b_1 to b_2 as ω increases from c_1 to c_2 .

4.0 Robust 2-sliding mode system

Before we present the design of sliding mode corrector, we give a 2-sliding mode system, and a Theorem is presented as follows.

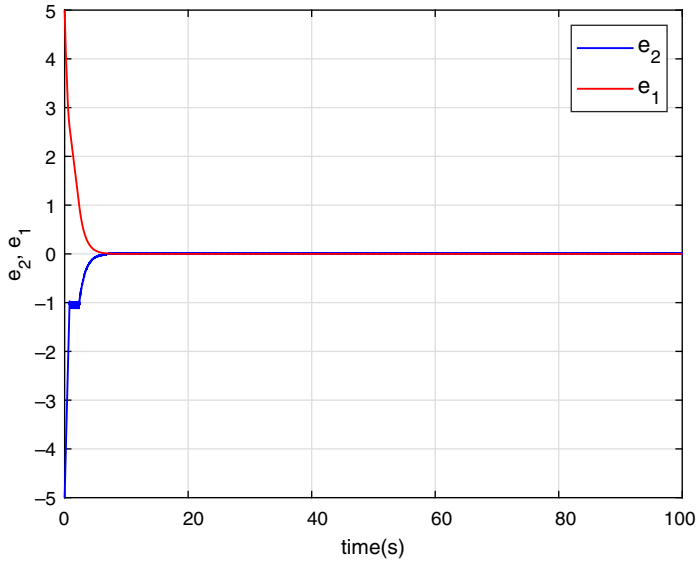


Figure 1. Sliding variables e_1 and e_2 .

Theorem 4.1 (sliding mode with prescribed linear convergence law): The 2-sliding mode system is as follows:

$$\begin{aligned} \dot{e}_1 &= e_2 \\ \dot{e}_2 &= \begin{cases} -e_2, & \text{if } |e_2| > 1; \\ -k_2 \text{sign}(e_2 + k_1 e_1), & \text{if } |e_2| \leq 1 \end{cases} \end{aligned} \tag{8a}$$

or

$$\begin{aligned} \dot{e}_1 &= e_2 \\ \dot{e}_2 &= \begin{cases} -k_3 \text{sign}(e_2), & \text{if } |e_2| > 1; \\ -k_2 \text{sign}(e_2 + k_1 e_1), & \text{if } |e_2| \leq 1 \end{cases} \end{aligned} \tag{8b}$$

where, e_1 and e_2 are the sliding variables; $k_2 > k_1 > 0$, and $k_3 > 0$. Then, we get the linear convergence law $\dot{e}_1 = -k_1 e_1$ (i.e. sliding surface $e_2 + k_1 e_1 = 0$), and the system (8a) or (8b) is exponentially stable, i.e.

$$\lim_{t \rightarrow \infty} e_1 = 0 \text{ and } \lim_{t \rightarrow \infty} e_2 = 0 \tag{9}$$

The proof of Theorem 4.1 is presented in Appendix. ■

In fact, for (8b), when $|e_2| > 1$, we use $\dot{e}_2 = -k_3 \text{sign}(e_2)$ for $\dot{e}_2 = -e_2$ to speed up e_2 convergence and overcome disturbance, where, $k_3 > 0$.

Simulation example (sliding mode with prescribed linear convergence law): For the sliding mode system (8b), we select $k_1 = 1$, $k_2 = 10$, and $k_3 = 5$. Then, we get e_1 and e_2 in Fig. 1. Figure 1 illustrates the fast convergence of e_1 and e_2 .

In the following, we give a robust 2-sliding mode system considering existence of multiple disturbances, and a Theorem is presented as follows.

Theorem 4.2 (robust 2-sliding mode): A 2-sliding mode system considering the unknown bounded disturbances is as follows:

$$\begin{aligned} \dot{e}_1 &= e_2 \\ \dot{e}_2 &= \begin{cases} -k_3 \text{sign}[e_2 - d_2(t)] - d_3(t), & \text{if } |e_2 - d_2(t)| > 1; \\ -k_2 \text{sign}[e_2 - d_2(t) + k_1(e_1 - d_1(t))] - d_4(t), & \text{if } |e_2 - d_2(t)| \leq 1 \end{cases} \end{aligned} \tag{10}$$

where, e_1 and e_2 are the sliding variables; the unknown bounded disturbances $d_i(t)$ satisfy $\sup_{t \in [0, \infty)} |d_i(t)| \leq L_i < \infty$ ($i = 1, 2, 3, 4$); $L_2 \ll 1$, and there exists a constant $\varepsilon > 0$ such that $\max \left\{ \frac{L_2}{L_1} \right\} \leq \varepsilon \ll 1$; $k_1 = 2\varepsilon^{1-r}$, where $r \in (0, \frac{1}{2}]$; $k_2 > k_1 + L_4$, and $k_3 > L_3$. Then, the effect of disturbances is rejected, and the variables e_1 and e_2 of system (10) are in the bounds as follows:

$$\lim_{t \rightarrow \infty} |e_1| \leq \rho(\omega_1)L_1; \quad \lim_{t \rightarrow \infty} |e_2| \leq L_2 \tag{11}$$

where, ω_1 is the angular frequency of disturbance $d_1(t)$; and the rejection ratio is expressed by

$$\rho(\omega_1) = \frac{1}{\sqrt{1 + \frac{1}{4}\varepsilon^{2r-2}\omega_1^2}} + \frac{1}{2}\varepsilon^r \tag{12}$$

The rejection ratio $\rho(\omega_1)$ is a monotonically decreasing function of $\omega_1 \in [0, \infty)$, and it satisfies:

- (i) In $[\omega_0, \infty)$, $\rho(\omega_1) : \varepsilon^r \rightarrow \frac{1}{2}\varepsilon^r$ as $\omega_1 : \omega_0 \rightarrow \infty$, where, $\omega_0 = 4\varepsilon^{1-2r}\sqrt{1 - \frac{1}{4}\varepsilon^{2r}}$;
- (ii) In (ω_c, ω_0) , $\rho(\omega_1) : 1 \rightarrow \varepsilon^r$ as $\omega_1 : \omega_c \rightarrow \omega_0$, where, $\omega_c = \frac{\varepsilon^{1-\frac{1}{2}r}\sqrt{4-\varepsilon^r}}{1-\frac{1}{2}\varepsilon^r} < 4\varepsilon^{1-\frac{1}{2}r} \ll 1$;
- (iii) In $[0, \omega_c]$, $\rho(\omega_1) : 1 + \frac{1}{2}\varepsilon^r \rightarrow 1$ (i.e. $\rho(\omega_1) \approx 1$ due to $0 < \varepsilon \ll 1$) as $\omega_1 : 0 \rightarrow \omega_c$, and this frequency band is sufficiently small due to $\omega_c \ll 1$.

The proof of Theorem 4.2 is presented in Appendix. ■

Remark 4.1: From $0 < \varepsilon \ll 1$ and $r \in (0, \frac{1}{2}]$, we can get that both the rejection ratio $\rho(\omega_1)$ in frequency band $[\omega_0, \infty)$ and the frequency ω_0 are small enough. Therefore, the disturbance $d_1(t)$ is reduced at very small rejection ratio in the large frequency band $[\omega_0, \infty)$. In fact, the disturbance bound L_2 in velocity sensing through Doppler effect is a few centimetres or a few millimetres, and the disturbance bound L_1 in position sensing is usually about a few metres or even tens of metres. Thus, the sensing accuracy inequality $\frac{L_2}{L_1} \ll 1$ holds, and there exists $\varepsilon > 0$ such that $\max \left\{ \frac{L_2}{L_1} \right\} \leq \varepsilon \ll 1$. When disturbance $d_1(t)$ becomes worse, i.e. L_1 increases, the inequality $\frac{L_2}{L_1} \leq \varepsilon \ll 1$ still holds. Therefore, the frequency band $[\omega_0, \infty)$ covers the low/mid/high frequency bands, and the disturbance $d_1(t)$ in position sensing in $[\omega_0, \infty)$ is rejected sufficiently by the corrector. Furthermore, the disturbance $d_1(t)$ can still be rejected largely in the other frequency bands.

In the following, we consider the position disturbance $d_1(t)$ is rejected to the maximum extent in a given frequency band, and the disturbance in the other bands can still be rejected largely. We will determine the corrector parametre k_1 to get the minimum value of the rejection ratio in the given frequency band $[\omega_{req}, \infty)$, and a Theorem is presented as follows.

Theorem 4.3 (sufficient disturbance rejection in given frequency band): The sliding mode system (10) is considered, where, the unknown bounded disturbances $d_i(t)$ satisfy $\sup_{t \in [0, \infty)} |d_i(t)| \leq L_i < \infty$ ($i = 1, 2, 3, 4$); $L_2 \ll 1$, and there exists a constant $\varepsilon > 0$ such that $\max \left\{ \frac{L_2}{L_1} \right\} \leq \varepsilon \ll 1$. For the a given $\omega_{req} > 0$, if we select $k_3 > L_3$, $k_2 > k_1 + L_4$ and $k_1 = 1/x_{\min}$, where, x_{\min} is the unique solution to

$$\omega_{req}^2 x_{\min} (1 + \omega_{req}^2 x_{\min}^2)^{-\frac{3}{2}} - \varepsilon = 0 \tag{13}$$

in the range $(\frac{1}{\sqrt{2\omega_{req}}}, \infty)$, then, the effect of disturbances is rejected, especially it is rejected sufficiently in the frequency band $[\omega_{req}, \infty)$, and the variables e_1 and e_2 of system (10) are in the bounds as follows:

$$\lim_{t \rightarrow \infty} |e_1| \leq \rho(\omega_1)L_1; \lim_{t \rightarrow \infty} |e_2| \leq L_2 \tag{14}$$

where, the rejection ratio is expressed by

$$\rho(\omega_1) = \frac{1}{\sqrt{1 + x_{\min}^2 \omega_1^2}} + \varepsilon \cdot x_{\min} \tag{15}$$

The rejection ratio $\rho(\omega_1)$ is a monotonically decreasing function of $\omega_1 \in [0, \infty)$, and it satisfies:

(i) In $[\omega_0, \infty)$, $\rho(\omega_1) : \rho_{\min} \rightarrow \varepsilon \cdot x_{\min}$ as $\omega_1 : \omega_{req} \rightarrow \infty$.

(ii) In (ω_c, ω_0) , $\rho(\omega_1) : 1 \rightarrow \rho_{\min}$ as $\omega_1 : \omega_c \rightarrow \omega_{req}$, where, $\omega_c = \frac{\sqrt{\frac{2\varepsilon}{x_{\min}}} \sqrt{1 - \frac{1}{2} \varepsilon x_{\min}}}{1 - \varepsilon x_{\min}}$.

(iii) In $[0, \omega_c]$, $\rho(\omega_1) : 1 + \varepsilon \cdot x_{\min} \rightarrow 1$ as $\omega_1 : 0 \rightarrow \omega_c$.

where,

$$\rho_{\min} = \frac{1}{\sqrt{1 + \omega_{req}^2 x_{\min}^2}} + \varepsilon \cdot x_{\min} \tag{16}$$

The proof of Theorem 4.3 is presented in Appendix. ■

5.0 Design of sliding mode corrector

According to Theorem 4.2, and considering disturbance in position sensing, a sliding mode corrector is designed to reject the disturbance, and a theorem is presented as follows.

Theorem 5.1 (sliding mode corrector): Suppose position measurement is $p_m(t) = p_0(t) + d_1(t)$, and velocity measurement is $v_m(t) = v_0(t) + d_2(t)$; $p_0(t)$ is the actual position, and $v_0(t)$ is the actual velocity; the unknown bounded disturbances $d_1(t)$ and $d_2(t)$ satisfy $\sup_{t \in [0, \infty)} |d_i(t)| \leq L_i < \infty$, where, $i = 1, 2$; $L_2 \ll 1$, and there exists a constant $\varepsilon > 0$ such that $\max \left\{ \frac{L_2}{L_1} \right\} \leq \varepsilon \ll 1$; $\sup_{t \in [0, \infty)} |\dot{v}_0(t)| \leq L_3 < \infty$. The sliding mode corrector is designed as follows:

$$\begin{aligned} \dot{x}_1 &= x_2 \\ \dot{x}_2 &= \begin{cases} -k_3 \text{sign} [x_2 - v_m(t)], & \text{if } |x_2 - v_m(t)| > 1; \\ -k_2 \text{sign} [x_2 - v_m(t) + k_1(x_1 - p_m(t))], & \text{if } |x_2 - v_m(t)| \leq 1 \end{cases} \end{aligned} \tag{17}$$

where, x_1 and x_2 are the corrector variables; the corrector parameters satisfy $k_1 = 2\varepsilon^{1-r}$ (where $r \in (0, \frac{1}{2}]$), $k_2 > k_1 + L_3$ and $k_3 > L_3$. Then, the disturbance $d_1(t)$ is rejected, and the corrector estimate outputs satisfy:

$$\lim_{t \rightarrow \infty} |x_1 - p_0(t)| \leq \rho(\omega_1)L_1; \lim_{t \rightarrow \infty} |x_2 - v_0(t)| \leq L_2 \tag{18}$$

where, ω_1 is the angular frequency of disturbance $d_1(t)$, and the rejection ratio is expressed by

$$\rho(\omega_1) = \frac{1}{\sqrt{1 + \frac{1}{4} \varepsilon^{2r-2} \omega_1^2}} + \frac{1}{2} \varepsilon^r \tag{19}$$

The rejection ratio $\rho(\omega_1)$ is a monotonically decreasing function of $\omega_1 \in [0, \infty)$, and it satisfies:

(i) In $[\omega_0, \infty)$, $\rho(\omega_1) : \varepsilon^r \rightarrow \frac{1}{2} \varepsilon^r$ as $\omega_1 : \omega_0 \rightarrow \infty$, where, $\omega_0 = 4\varepsilon^{1-2r} \sqrt{1 - \frac{1}{4} \varepsilon^{2r}}$;

(ii) In (ω_c, ω_0) , $\rho(\omega_1) : 1 \rightarrow \varepsilon^r$ as $\omega_1 : \omega_c \rightarrow \omega_0$, where, $\omega_c = \frac{\varepsilon^{1-\frac{1}{2}r} \sqrt{4 - \varepsilon^r}}{1 - \frac{1}{2} \varepsilon^r} < 4\varepsilon^{1-\frac{1}{2}r} \ll 1$;

(iii) In $[0, \omega_c]$, $\rho(\omega_1) : 1 + \frac{1}{2}\varepsilon^r \rightarrow 1$ (i.e. $\rho(\omega_1) \approx 1$) as $\omega_1 : 0 \rightarrow \omega_c$. This frequency band is sufficiently small due to $\omega_c \ll 1$.

The proof of Theorem 5.1 is presented in Appendix. ■

Remark 5.1 (analysis of corrector (17)): The sensing accuracy inequality $0 < \varepsilon \ll 1$ and $r \in (0, \frac{1}{2}]$ guarantee that the rejection ratio $\rho(\omega_1)$ in frequency band $[\omega_0, \infty)$ is small enough, and $[\omega_0, \infty)$ covers the low/mid/high frequency bands. Therefore, the disturbance $d_1(t)$ in $[\omega_0, \infty)$ can be rejected sufficiently by the corrector. Furthermore, the disturbance $d_1(t)$ in the low frequency band (ω_c, ω_0) is still reduced largely. Only the approximate constant disturbances in the extreme low-frequency band $[0, \omega_c]$ are not rejected. In fact, signals in the extreme low-frequency band $[0, \omega_c]$ is approximate constant due to sufficiently small $\omega_c \ll 1$. Therefore, the position disturbance $d_1(t)$ can be rejected sufficiently by the corrector even when the disturbance frequency covers low/mid/high frequency bands.

From Theorem 4.3, considering sufficient disturbance rejection in a given frequency band, we get the optimal sliding mode corrector, and a theorem is presented as follows.

Theorem 5.2 (optimal sliding mode corrector): The corrector (17) and the measurement signals in Theorem 5.1 are considered, where, the unknown bounded disturbances $d_i(t)$ satisfy $\sup_{t \in [0, \infty)} |d_i(t)| \leq L_i < \infty$ ($i = 1, 2$); $L_2 \ll 1$, and there exists a constant $\varepsilon > 0$ such that $\max \left\{ \frac{L_2}{L_1} \right\} \leq \varepsilon \ll 1$; $\sup_{t \in [0, \infty)} |\dot{v}_0(t)| \leq L_3 < \infty$. For the a given $\omega_{req} > 0$, if we select $k_3 > L_3$, $k_2 > k_1 + L_3$ and $k_1 = 1/x_{min}$, where, x_{min} is the unique solution to

$$\omega_{req}^2 x_{min} (1 + \omega_{req}^2 x_{min}^2)^{-\frac{3}{2}} - \varepsilon = 0 \tag{20}$$

in the range $(\frac{1}{\sqrt{2}\omega_{req}}, \infty)$, then, the disturbance $d_1(t)$ is rejected, especially it is rejected sufficiently in the frequency band $[\omega_{req}, \infty)$, and the corrector estimate outputs satisfy:

$$\lim_{t \rightarrow \infty} |x_1 - p_0(t)| \leq \rho(\omega_1)L_1; \lim_{t \rightarrow \infty} |x_2 - v_0(t)| \leq L_2 \tag{21}$$

where, the rejection ratio is expressed by

$$\rho(\omega_1) = \frac{1}{\sqrt{1 + x_{min}^2 \omega_1^2}} + \varepsilon \cdot x_{min} \tag{22}$$

The rejection ratio $\rho(\omega_1)$ is a monotonically decreasing function of $\omega_1 \in [0, \infty)$, and it satisfies:

- (i) In $[\omega_{req}, \infty)$, $\rho(\omega_1) : \rho_{min} \rightarrow \varepsilon \cdot x_{min}$ as $\omega_1 : \omega_{req} \rightarrow \infty$.
- (ii) In (ω_c, ω_{req}) , $\rho(\omega_1) : 1 \rightarrow \rho_{min}$ as $\omega_1 : \omega_c \rightarrow \omega_{req}$, where, $\omega_c = \frac{\sqrt{\frac{2\varepsilon}{x_{min}}}\sqrt{1 - \frac{1}{2}\varepsilon x_{min}}}{1 - \varepsilon \cdot x_{min}}$.
- (iii) In $[0, \omega_c]$, $\rho(\omega_1) : 1 + \varepsilon \cdot x_{min} \rightarrow 1$ as $\omega_1 : 0 \rightarrow \omega_c$.

where,

$$\rho_{min} = \frac{1}{\sqrt{1 + \omega_{req}^2 x_{min}^2}} + \varepsilon \cdot x_{min} \tag{23}$$

According to Theorem 4.3 and the system error (123) in the proof of Theorem 5.1, we can get the bounds of the correction errors in (21). This concludes the proof of Theorem 5.2. ■

Remark 5.2 (parametres regulation of corrector (17)):

- (1) The selection of $k_3 > L_3$, $k_2 > k_1 + L_3$ and $k_1 = 2\varepsilon^{1-r}$ (where, $\max \left\{ \frac{L_2}{L_1} \right\} \leq \varepsilon \ll 1$ and $r \in (0, \frac{1}{2}]$) makes the corrector stable: $k_3 > L_3$ and $k_2 > k_1 + L_3$ make the corrector estimate errors satisfy the convergence law (90); $k_1 = 2\varepsilon^{1-r}$ makes the sliding surface stable, and it further reduces the corrector estimate error.

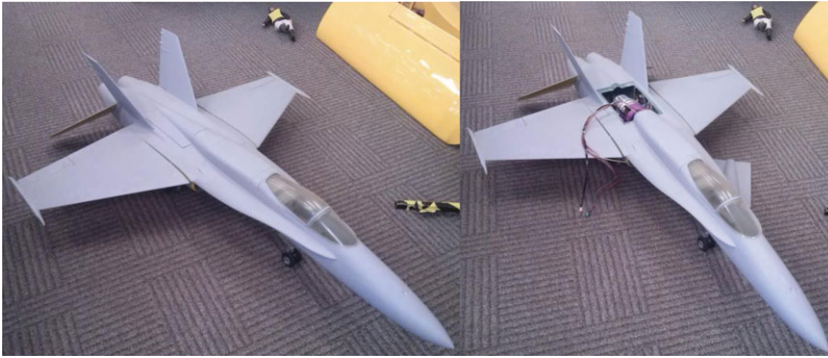


Figure 2. Jet UAV prototype.

- (2) The upper-bound of sensor accuracy ratio $0 < \varepsilon \ll 1$ and $r \in (0, \frac{1}{2}]$ make the rejection ratio $\rho(\omega_1)$ in frequency band $[\omega_0, \infty)$ and the frequency ω_0 sufficiently small, and the sufficiently rejectable frequency $\omega_1 \in [\omega_0, \infty)$ may be in the low/mid/high frequency bands.
- (3) Furthermore, the selection of parametre r affects the rejection ratio $\rho(\omega_1)$ and the sufficiently rejectable frequency band $[\omega_0, \infty)$. In fact:
 - (i) Due to $0 < \varepsilon \ll 1$, the smaller r is, the bigger $\varepsilon^r \in (0, 1)$ is, and ω_0 decreases. Therefore, the frequency band $[\omega_0, \infty)$ becomes relatively wider.
 - (ii) Conversely, the larger r is, the smaller $\varepsilon^r \in (0, 1)$ is, and ω_0 increases. Therefore, the frequency band $[\omega_0, \infty)$ is reduced.
 - (iii) Minimum range and minimum value of $\rho(\omega_1)$: From $\rho(\omega_1) = \frac{1}{\sqrt{1 + \frac{1}{4}\varepsilon^{2r-2}\omega_1^2}} + \frac{1}{2}\varepsilon^r$, we know that $\rho(\omega_1) \in (\frac{1}{2}\varepsilon^r, 1 + \frac{1}{2}\varepsilon^r]$ when $\omega_1 \in [0, \infty)$. Due to $0 < \varepsilon \ll 1$ and $r \in (0, \frac{1}{2}]$, when we select $r = \frac{1}{2}$, we can get the minimum value of $\min\{\varepsilon^r\} = \varepsilon^{\frac{1}{2}}$. Therefore, the minimum value of $\rho(\omega_1)$ is $\min\{\rho(\omega_1)\} = \frac{1}{2}\varepsilon^{\frac{1}{2}}$, and the minimum range is $\rho(\omega_1) \in (\frac{1}{2}\varepsilon^{\frac{1}{2}}, 1 + \frac{1}{2}\varepsilon^{\frac{1}{2}}]$ when $\omega_1 \in [0, \infty)$.

6.0 Application to jet UAV navigation and control

An RC-model-based F/A-18 Hornet prototype is used [17], which is shown in Fig. 2, and the forces and torques of UAV are described in Fig. 3.

6.1 Modelling of jet UAV flight dynamics

For the UAV trajectory tracking control, the modelling is considered in the earth-fixed frame [23]. Furthermore, the constructed model is fit for observer design to estimate system uncertainties.

Let $\Gamma = (E_x, E_y, E_z)$ denote the earth-fixed frame, and $\Lambda = (E_x^b, E_y^b, E_z^b)$ denote the body frame of the UAV. $\Theta_\Gamma = [\phi \theta \psi]^T \in \mathbb{R}^3$ describes the UAV roll, pitch and yaw angles (Euler angles), and $\Omega_\Gamma = [\dot{\phi} \dot{\theta} \dot{\psi}]^T$. We use s_θ for $\sin \theta$ and c_θ for $\cos \theta$. $R_{\Gamma\Lambda}$ is the transformation matrix representing the orientation of the body frame Λ with respect to the earth-fixed frame Γ :

$$R_{\Gamma\Lambda} = \begin{bmatrix} c_\theta c_\psi & c_\psi s_\theta s_\phi - s_\psi c_\phi & c_\psi s_\theta c_\phi + s_\psi s_\phi \\ c_\theta s_\psi & s_\psi s_\theta s_\phi + c_\psi c_\phi & s_\psi s_\theta c_\phi - c_\psi s_\phi \\ -s_\theta & s_\phi c_\theta & c_\phi c_\theta \end{bmatrix} \tag{24}$$

Let α and β be the angle-of-attack and the sideslip angle, respectively, we can get

$$\alpha = \theta - \arctan^{-1}(W/U), \beta = \arcsin^{-1}(V/V_T) \tag{25}$$

where, $v_\Lambda = (U, V, W)$ is the linear velocity in body frame Λ , and $V_T = \sqrt{U^2 + V^2 + W^2}$.

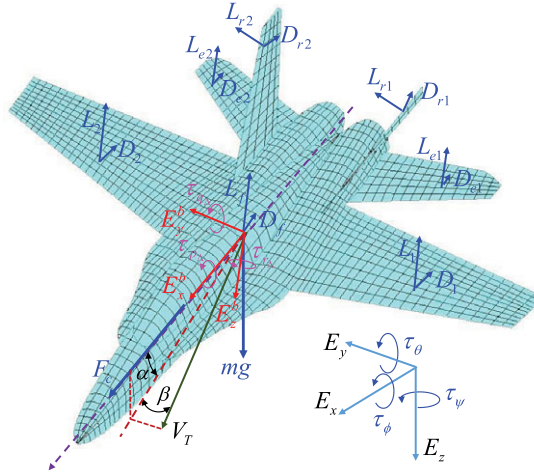


Figure 3. UAV aerodynamic mesh, forces and moments.

Define $p_\Gamma = (x, y, z)$ and $v_\Gamma = (\dot{x}, \dot{y}, \dot{z})$ as the position and velocity vectors of centre of gravity, respectively, relative to the earth-fixed frame Γ ; Ω_Λ is the angular rate vector of the airframe expressed in the body frame Λ ; $m \in \Re$ is the UAV mass, and $J = \text{diag}\{J_{xb}, J_{yb}, J_{zb}\} \in \Re^{3 \times 3}$ is the UAV inertia matrix. Then, the dynamic equations for the jet UAV subjected to force $F \in \Re^3$ and torque $\tau \in \Re^3$ are given by

$$\begin{aligned} \dot{p}_\Gamma &= v_\Gamma \\ m \cdot \dot{v}_\Gamma &= F + mgE_z \\ J \cdot \dot{\Omega}_\Lambda &= -\Omega_\Lambda \times (J\Omega_\Lambda) + \tau \end{aligned} \tag{26}$$

where, $E_z = [0 \ 0 \ 1]^T$. The relation between the angular rate vector $\Omega_\Lambda = [p_\Lambda \ q_\Lambda \ r_\Lambda]^T$ and the Euler angle derivative vector $\Omega_\Gamma = [\dot{\phi} \ \dot{\theta} \ \dot{\psi}]^T$ is given by

$$\Omega_\Lambda = \mathbb{Z}\Omega_\Gamma \text{ or } \Omega_\Gamma = \mathbb{Z}^{-1}\Omega_\Lambda \tag{27}$$

where,

$$\mathbb{Z} = \begin{bmatrix} 1 & 0 & -s_\theta \\ 0 & c_\phi & s_\phi c_\theta \\ 0 & -s_\phi & c_\phi c_\theta \end{bmatrix}, \mathbb{Z}^{-1} = \begin{bmatrix} 1 & s_\phi s_\theta / c_\theta & c_\phi s_\theta / c_\theta \\ 0 & c_\phi & -s_\phi \\ 0 & s_\phi / c_\theta & c_\phi / c_\theta \end{bmatrix} \tag{28}$$

The total external force F consists of the thrust F_{jet} generated by the jet engine, aerodynamic forces on the fixed wing F_w , aerodynamic forces on the fuselage F_f , the forces created by the rudders F_r , the forces created by the elevators F_e , and uncertainties and external disturbances F_d . These forces are expressed in body frame Λ , and they are transformed by $R_{\Gamma\Lambda}$ to be expressed in the earth-fixed frame Γ as follows:

$$F = R_{\Gamma\Lambda}(F_{jet} + F_w + F_f + F_r + F_e + F_d) \tag{29}$$

The total moment τ consists of the moments created by the fixed wings τ_w , the moments created by the rudders τ_r , the moments created by the elevators τ_e , and moments due to the uncertainties and external disturbances τ_d :

$$\tau = \tau_w + \tau_r + \tau_e + \tau_d \tag{30}$$

The aerodynamic parameters of the UAV are from [17]. The CFD (computational fluid dynamics) simulation was performed, and the results from the wind tunnel tests were compared. For the boundary conditions, the method of free-stream boundary condition based on Riemann invariants was utilised

[28]: no-slip viscous flow condition; the linearised one-dimensional Euler equations; the free-stream values for determination of the value of the Riemann invariants; and the symmetrical boundary condition for the symmetrical UAV. The ANSYS Fluent was used for the CFD simulation, and the design steps included meshing fluid field, fluent simulation and post-processing [29].

(1) *Thrust by jet engine*: The thrust of engine in body frame is expressed by

$$F_{jet} = [F_c \ 0 \ 0]^T \tag{31}$$

(2) *Aerodynamics of fixed wings*

Define $q = 0.5\rho(U^2 + W^2)$, where, ρ is the air density. The lift and drag forces generated by the fixed wings are, respectively

$$\begin{aligned} L_i &= qS_w C_{Li}, C_{Li} = C_{L0} + C_{L\alpha}\alpha + C_{L\delta_i}\delta_i \\ D_i &= qS_w C_{Di}, C_{Di} = C_{D0} + C_{Di}^2/(\pi A_w e_w) \\ e_w &= 1.78(1 - 0.045A_w^{0.68}) - 0.46 \end{aligned} \tag{32}$$

where $i = 1, 2$; S_w is the area of the half wing; C_{L0} is the lift coefficient when the angle-of-attack α equals zero; $C_{L\alpha}$ is the lift coefficient due to the angle-of-attack α ; δ_i is the aileron deflection, and $C_{L\delta_i}$ is the lift coefficient due to the aileron deflection δ_i ; C_{D0} is the drag coefficient when $\alpha = \delta_i = 0$; A_w is the aspect ratio of the fixed wing; e_w is the value of the Oswald’s efficiency factor. The expression of lift and drag coefficients is considered as valid for low angles of attack.

Then the aerodynamic force vector F_w on the fixed wings in body frame can be written as

$$F_w = \begin{bmatrix} (L_1 + L_2)s_\alpha - (D_1 + D_2)c_\alpha \\ 0 \\ -(L_1 + L_2)c_\alpha - (D_1 + D_2)s_\alpha \end{bmatrix} \tag{33}$$

The fixed-wing moment τ_w includes the aerodynamic moment τ_{wa} and control torque τ_{wc} around the body axis E_x^b , i.e. $\tau_w = \tau_{wa} + \tau_{wc}$, where,

$$\tau_{wa} = \begin{bmatrix} l_w(D_1 - D_2)s_\alpha \\ l_c[(L_2 + L_1)c_\alpha + (D_2 + D_1)s_\alpha] \\ l_w[(L_1 - L_2)s_\alpha + (D_2 - D_1)c_\alpha] \end{bmatrix} \tag{34}$$

and

$$\tau_{wc} = \begin{bmatrix} l_w q S_w C_{L\delta_{1,2}}(\delta_1 - \delta_2)c_\alpha \\ 0 \\ 0 \end{bmatrix} \tag{35}$$

(3) *Fuselage*

The parametres of fuselage lift and drag are described as follows:

$$\begin{aligned} L_f &= qS_f C_{lf}, C_{lf} = C_{lf\alpha}\alpha, \\ D_f &= qS_f C_{df}, C_{df} = C_{df0} + C_{df\alpha}\alpha \end{aligned} \tag{36}$$

where, S_f is the fuselage equivalent cross-sectional area; L_f and D_f are the lift and drag forces generated by the fuselage, respectively; C_{lf} is the lift coefficient; C_{df} is the drag coefficient; C_{df0} is the constant in the coefficient of drag force. Then the force vector F_f on the fuselage in body frame is expressed by

$$F_f = \begin{bmatrix} L_f s_\alpha - D_f c_\alpha \\ 0 \\ -L_f c_\alpha - D_f s_\alpha \end{bmatrix} \tag{37}$$

(4) Elevator

The parametres of elevator lift and drag are described as follows:

$$\begin{aligned}
 L_e &= qS_e C_{le}, C_{le} = C_{le\alpha}(\alpha + \delta_e) \\
 D_e &= qS_e C_{de}, C_{de} = C_{de0} + C_{le}^2 / (\pi A_e e_e) \\
 e_e &= 1.78(1 - 0.045A_e^{0.68}) - 0.46
 \end{aligned}
 \tag{38}$$

where S_e is the area of the elevator, δ_e is the elevator deflection; $C_{le\alpha}$ is the lift coefficient due to the angle-of-attack α and the deflection δ_e ; C_{de0} is the drag coefficient when $\alpha + \delta_e = 0$; A_e is the aspect ratio of the elevator; e_e is the value of the Oswald's efficiency factor. Then the force vector F_e on the elevator in body frame is expressed by

$$F_e = \begin{bmatrix} L_e s_\alpha - D_e c_\alpha \\ 0 \\ -L_e c_\alpha - D_e s_\alpha \end{bmatrix}
 \tag{39}$$

The elevator moment τ_e includes the aerodynamic moment τ_{ea} and control torque τ_{ec} in the body axis E_y^b , i.e. $\tau_e = \tau_{ea} + \tau_{ec}$, where,

$$\tau_{ea} = \begin{bmatrix} 0 \\ -l_e D_e s_\alpha \\ 0 \end{bmatrix}
 \tag{40}$$

and

$$\tau_{ec} = \begin{bmatrix} 0 \\ -l_e q S_e C_{le\alpha}(\alpha + \delta_e) c_\alpha \\ 0 \end{bmatrix}
 \tag{41}$$

(5) Rudders

Define $\bar{q} = 0.5\rho(U^2 + V^2)$. The lift and drag forces generated by the rudders, respectively

$$\begin{aligned}
 L_r &= \bar{q}S_r C_{lr}, C_{lr} = C_{lr\beta}\beta + C_{lr\delta_r}\delta_r \\
 D_r &= \bar{q}S_r C_{dr}, C_{dr} = C_{dr0} + C_{lr}^2 / (\pi A_r e_r) \\
 e_r &= 1.78(1 - 0.045A_r^{0.68}) - 0.46
 \end{aligned}
 \tag{42}$$

where, S_r is the area of the rudders; $C_{lr\beta}$ is the lift coefficient due to the sideslip angle β ; δ_r is the rudder deflection, and $C_{lr\delta_r}$ is the lift coefficient due to the deflection δ_r ; C_{dr0} is the drag coefficient when $\beta = \delta_r = 0$; A_r is the aspect ratio of the rudder; e_r is the value of the Oswald's efficiency factor. Then the aerodynamic force vector F_r on the rudders in body frame can be expressed by

$$F_r = \begin{bmatrix} L_r s_\beta - D_r c_\beta \\ L_r c_\beta + D_r s_\beta \\ 0 \end{bmatrix}
 \tag{43}$$

The rudder moment τ_r includes the aerodynamic moment τ_{ra} and control torque τ_{rc} in body axis E_z^b , i.e. $\tau_r = \tau_{ra} + \tau_{rc}$, where,

$$\tau_{ra} = \begin{bmatrix} 0 \\ 0 \\ l_r D_r s_\beta \end{bmatrix}
 \tag{44}$$

and

$$\tau_{rc} = \begin{bmatrix} 0 \\ 0 \\ l_r \bar{q} S_r (C_{lr\beta}\beta + C_{lr\delta_r}\delta_r) c_\beta \end{bmatrix}
 \tag{45}$$

(6) UAV motion equations in the earth-fixed frame considering system uncertainties

According to [23], from (27) and (26), we get

$$\begin{aligned} \dot{\Omega}_\Gamma &= (\mathbb{Z}^{-1})' \dot{\Omega}_\Lambda + \mathbb{Z}^{-1} \dot{\Omega}_\Lambda \\ &= (\mathbb{Z}^{-1})' \mathbb{Z} \Omega_\Gamma - \mathbb{Z}^{-1} J^{-1} [\mathbb{Z} \Omega_\Gamma \times (J \mathbb{Z} \Omega_\Gamma)] + \mathbb{Z}^{-1} J^{-1} \tau \end{aligned} \tag{46}$$

The total moment τ can be categorised into the control torque τ_c , uncertain moment τ_d and other moments τ_{other} , i.e.

$$\tau = \tau_c + \tau_{other} + \tau_d \tag{47}$$

From (35), (41) and (45), we get

$$\tau_c = \tau_{wc} + \tau_{ec} + \tau_{rc} \tag{48}$$

and from (34), (40) and (44), we get

$$\tau_{other} = \tau_{wa} + \tau_{ea} + \tau_{ra} \tag{49}$$

In system (46), considering (47), we define

$$(\mathbb{Z}^{-1})' \mathbb{Z} \Omega_\Gamma - \mathbb{Z}^{-1} J^{-1} [\mathbb{Z} \Omega_\Gamma \times (J \mathbb{Z} \Omega_\Gamma)] + \mathbb{Z}^{-1} J^{-1} \tau_{other} \stackrel{\text{define}}{=} \begin{bmatrix} a_\phi(\phi, \theta, \psi, \dot{\phi}, \dot{\theta}, \dot{\psi}, \alpha, \beta) \\ a_\theta(\phi, \theta, \psi, \dot{\phi}, \dot{\theta}, \dot{\psi}, \alpha, \beta) \\ a_\psi(\phi, \theta, \psi, \dot{\phi}, \dot{\theta}, \dot{\psi}, \alpha, \beta) \end{bmatrix} \tag{50}$$

$$\mathbb{Z}^{-1} J^{-1} \tau_c \stackrel{\text{define}}{=} [\tau_\phi \quad \tau_\theta \quad \tau_\psi]^T \tag{51}$$

In (29), we define

$$R_{\Gamma\Lambda}(F_w + F_f + F_r + F_e)/m \stackrel{\text{define}}{=} \begin{bmatrix} F_{xa}(\phi, \theta, \psi, \alpha, \beta) \\ F_{ya}(\phi, \theta, \psi, \alpha, \beta) \\ F_{za}(\phi, \theta, \psi, \alpha, \beta) \end{bmatrix} \tag{52}$$

Then, the jet UAV motion equations written in terms of the centre of mass C in the earth-fixed frame are

$$\begin{aligned} \ddot{x} &= c_\theta c_\psi F_c/m + F_{xa}(\phi, \theta, \psi, \alpha, \beta) + \Delta_x \\ \ddot{y} &= c_\theta s_\psi F_c/m + F_{ya}(\phi, \theta, \psi, \alpha, \beta) + \Delta_y \\ \ddot{z} &= -s_\theta F_c/m + F_{za}(\phi, \theta, \psi, \alpha, \beta) + g + \Delta_z \end{aligned} \tag{53}$$

$$\begin{aligned} \ddot{\phi} &= a_\phi(\phi, \theta, \psi, \dot{\phi}, \dot{\theta}, \dot{\psi}, \alpha, \beta) + \tau_\phi + \Delta_\phi \\ \ddot{\theta} &= a_\theta(\phi, \theta, \psi, \dot{\phi}, \dot{\theta}, \dot{\psi}, \alpha, \beta) + \tau_\theta + \Delta_\theta \\ \ddot{\psi} &= a_\psi(\phi, \theta, \psi, \dot{\phi}, \dot{\theta}, \dot{\psi}, \alpha, \beta) + \tau_\psi + \Delta_\psi \end{aligned} \tag{54}$$

where, m is the mass of the UAV; g is the gravity acceleration; $(\Delta_x, \Delta_y, \Delta_z)$ and $(\Delta_\phi, \Delta_\theta, \Delta_\psi)$ are the bounded uncertainties in the position and attitude dynamics, respectively; τ_ϕ, τ_θ and τ_ψ are the control torques for roll, pitch and yaw dynamics, respectively, defined in (51).

6.2 Measurements

For the jet UAV, a GPS receiver provides the global position and the velocity. An IMU gives the attitude angle and angular velocity. The measurement outputs are expressed by

$$y_{*1} = * + d_{*1}(t), y_{*2} = \dot{*} + d_{*2}(t) \tag{55}$$

where, $*_i = \{x, y, z, \phi, \theta, \psi\}$, and $\dot{*} = \{\dot{x}, \dot{y}, \dot{z}, \dot{\phi}, \dot{\theta}, \dot{\psi}\}$; $d_{*1}(t)$ denotes the disturbances in position and angle measurements, and $\sup_{t \in [0, \infty)} |d_{*1}(t)| \leq L_{*1} < \infty$; $d_{*2}(t)$ denotes the disturbances in the

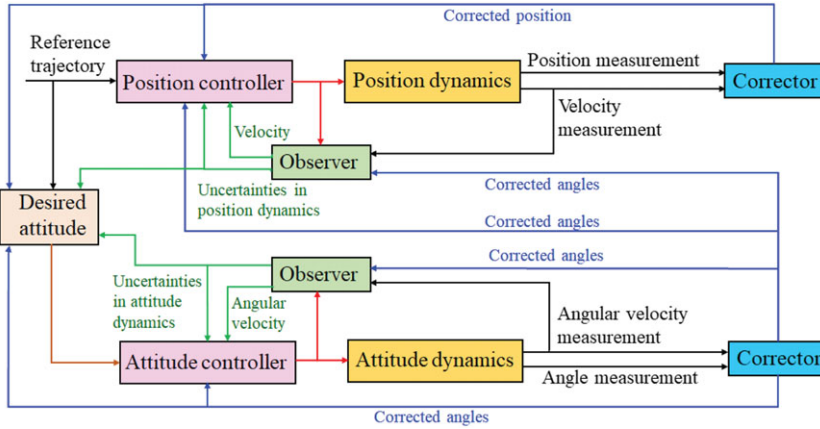


Figure 4. Scheme of control system.

measurements of flying velocity and angular velocity, and $\sup_{t \in [0, \infty)} |d_{*2}(t)| \leq L_{*2} < \infty$; $L_{*2} \ll 1$, and $\max \left\{ \frac{L_{*1}}{L_{*2}} \right\} \leq \varepsilon_* \ll 1$. The corrector (17) is used to reject the measurement disturbances and to estimate the actual $(x, y, z, \phi, \theta, \psi)$.

6.3 Controller design

In this section, the control laws are derived for UAV trajectory tracking and attitude stabilisation. The position, attitude and system uncertainties are reconstructed by the presented corrector and an existing extended state observer.

The scheme of control system with correction and estimation is shown in Fig. 4: (1) the correctors estimate position and attitude angles, and the disturbances are rejected from the measurements; (2) the extended state observers estimate the uncertainties in position and attitude dynamics, respectively; (3) according to the reference trajectory and estimation from the correctors and observers, the position controller drives the position dynamics; (4) from the estimation of position, attitude, uncertainties and the reference trajectory, the desired attitude is determined; (5) according to the desired attitude and estimation from the correctors and observers, the attitude controller drives the attitude dynamics.

(1) Error systems

Suppose the reference trajectory and its finite order derivatives are bounded, and can be generated directly. For the reference trajectory $X_d = (x_d, y_d, z_d)$, let $e_x = x - x_d$, $e_y = y - y_d$, and $e_z = z - z_d$, then the system error for position dynamics (53) is

$$\ddot{e}_p = u_p + \Xi_p + \Delta_p \tag{56}$$

where,

$$e_p = \begin{bmatrix} e_x \\ e_y \\ e_z \end{bmatrix}, u_p = \begin{bmatrix} u_{px} \\ u_{py} \\ u_{pz} \end{bmatrix} = \begin{bmatrix} c_\theta c_\psi \\ c_\theta s_\psi \\ -s_\theta \end{bmatrix} F_c/m,$$

$$\Xi_p = \begin{bmatrix} F_{xa}(\phi, \theta, \psi, \alpha, \beta) - \ddot{x}_d \\ F_{ya}(\phi, \theta, \psi, \alpha, \beta) - \ddot{y}_d \\ F_{za}(\phi, \theta, \psi, \alpha, \beta) + g - \ddot{z}_d \end{bmatrix}, \Delta_p = \begin{bmatrix} \Delta_x \\ \Delta_y \\ \Delta_z \end{bmatrix} \tag{57}$$

For the desired attitude angle $\Theta_d = (\phi_d, \theta_d, \psi_d)$, let $e_\phi = \phi - \phi_d$, $e_\theta = \theta - \theta_d$, and $e_\psi = \psi - \psi_d$, then the system error for attitude dynamics (54) is

$$\ddot{e}_a = u_a + \Xi_a + \Delta_a \tag{58}$$

where,

$$e_a = \begin{bmatrix} e_\phi \\ e_\theta \\ e_\psi \end{bmatrix}, u_a = \begin{bmatrix} \tau_\phi \\ \tau_\theta \\ \tau_\psi \end{bmatrix}, \Delta_a = \begin{bmatrix} \Delta_\phi \\ \Delta_\theta \\ \Delta_\psi \end{bmatrix},$$

$$\Xi_a = \begin{bmatrix} a_\phi(\phi, \theta, \psi, \dot{\phi}, \dot{\theta}, \dot{\psi}, \alpha, \beta) - \ddot{\phi}_d \\ a_\theta(\phi, \theta, \psi, \dot{\phi}, \dot{\theta}, \dot{\psi}, \alpha, \beta) - \ddot{\theta}_d \\ a_\psi(\phi, \theta, \psi, \dot{\phi}, \dot{\theta}, \dot{\psi}, \alpha, \beta) - \ddot{\psi}_d \end{bmatrix} \tag{59}$$

(2) Extended state observers for the uncertainties Δ_p and Δ_a

The extended state observers [24] are used to estimate the uncertainties in position dynamics (53) and attitude dynamics (54). For the observers, the measurements of flying velocity and angular velocity $y_{*2} = \dot{*} + d_{*2}(t)$ (where, $*$ = $\{\dot{x}, \dot{y}, \dot{z}, \dot{\phi}, \dot{\theta}, \dot{\psi}\}$) are the input signals. Then, the uncertainty $\Delta_p = [\Delta_x, \Delta_y, \Delta_z]^T$ in the position dynamics and the uncertainty $\Delta_a = [\Delta_\phi, \Delta_\theta, \Delta_\psi]^T$ in the attitude dynamics are estimated.

The continuous extended state observers can provide smooth and accurate estimations of the uncertainties in the system dynamics, reducing high-frequency vibrations.

The following extended state observers are used [24]:

$$\begin{aligned} \dot{x}_{*1} &= x_{*2} - \lambda_{*1}|x_{*1} - y_{*2}|^{\frac{1+\alpha_*}{2}} \text{sign}(x_{*1} - y_{*2}) + H_* \\ \dot{x}_{*2} &= -\lambda_{*2}|x_{*1} - y_{*2}|^{\alpha_*} \text{sign}(x_{*1} - y_{*2}) \end{aligned} \tag{60}$$

From Theorem 1 in, [24] there exist a finite time $t_s > 0$ such that, for $t \geq t_s$,

$$x_{*1} = \dot{*}, x_{*2} = \Delta_* \tag{61}$$

where, $*$ = $\{x, y, z, \psi, \theta, \phi\}$ and $\dot{*}$ = $\{\dot{x}, \dot{y}, \dot{z}, \dot{\phi}, \dot{\theta}, \dot{\psi}\}$; $\lambda_{*1}, \lambda_{*2} > 0$, and $\alpha_* \in (0, 1)$; The measurement y_{*2} defined in (55) is the observer input signal;

$$\begin{aligned} H_x &= u_{px} + F_{xa}(\widehat{\phi}, \widehat{\theta}, \widehat{\psi}, \alpha, \beta) \\ H_y &= u_{py} + F_{ya}(\widehat{\phi}, \widehat{\theta}, \widehat{\psi}, \alpha, \beta) \\ H_z &= u_{pz} + F_{za}(\widehat{\phi}, \widehat{\theta}, \widehat{\psi}, \alpha, \beta) - g \\ H_\phi &= \tau_\phi + a_\phi(\widehat{\phi}, \widehat{\theta}, \widehat{\psi}, \dot{\phi}, \dot{\theta}, \dot{\psi}, \alpha, \beta) \\ H_\theta &= \tau_\theta + a_\theta(\widehat{\phi}, \widehat{\theta}, \widehat{\psi}, \dot{\phi}, \dot{\theta}, \dot{\psi}, \alpha, \beta) \\ H_\psi &= \tau_\psi + a_\psi(\widehat{\phi}, \widehat{\theta}, \widehat{\psi}, \dot{\phi}, \dot{\theta}, \dot{\psi}, \alpha, \beta) \end{aligned} \tag{62}$$

and $(\widehat{\phi}, \widehat{\theta}, \widehat{\psi})$ are from the outputs of the sliding mode correctors. From (60) and (61), we get

$$\widehat{\Delta}_p = [x_{x2} x_{y2} x_{z2}]^T \tag{63}$$

and

$$\widehat{\Delta}_a = [x_{\psi2} x_{\theta2} x_{\phi2}]^T \tag{64}$$

(3) Controller design for position dynamics

For position dynamics (53), to track the reference trajectory $X_d = (x_d, y_d, z_d)$, when we select the following controller, the position system error (56) will converge asymptotically to zero:

$$u_p = -\widehat{\Xi}_p - \widehat{\Delta}_p - k_{p1}\widehat{e}_p - k_{p2}\dot{\widehat{e}}_p \tag{65}$$

where $\widehat{e}_x = \widehat{x} - x_d, \widehat{e}_y = \widehat{y} - y_d, \widehat{e}_z = \widehat{z} - z_d, \widehat{e}_x = \widehat{x} - \dot{x}_d, \widehat{e}_y = \widehat{y} - \dot{y}_d, \widehat{e}_z = \widehat{z} - \dot{z}_d; k_{p1}, k_{p2} > 0; (\widehat{x}, \widehat{y}, \widehat{z}, \widehat{\dot{x}}, \widehat{\dot{y}}, \widehat{\dot{z}}, \widehat{\phi}, \widehat{\theta}, \widehat{\psi})$ are from the outputs of the correctors; $\widehat{\Delta}_p$ is from the outputs of the extended state observer; and

$$\widehat{e}_p = \begin{bmatrix} \widehat{e}_x \\ \widehat{e}_y \\ \widehat{e}_z \end{bmatrix}, \widehat{\dot{e}}_p = \begin{bmatrix} \widehat{\dot{e}}_x \\ \widehat{\dot{e}}_y \\ \widehat{\dot{e}}_z \end{bmatrix},$$

$$\widehat{\Xi}_p = \begin{bmatrix} F_{xa}(\widehat{\phi}, \widehat{\theta}, \widehat{\psi}, \alpha, \beta) - \ddot{x}_d \\ F_{ya}(\widehat{\phi}, \widehat{\theta}, \widehat{\psi}, \alpha, \beta) - \ddot{y}_d \\ F_{za}(\widehat{\phi}, \widehat{\theta}, \widehat{\psi}, \alpha, \beta) - g - \ddot{z}_d \end{bmatrix} \tag{66}$$

From (57), we get the engine thrust

$$F_c = m \|u_p\|_2 = m \sqrt{u_{px}^2 + u_{py}^2 + u_{pz}^2} \tag{67}$$

(4) Desired attitude angles

From (56) and (65), we get

$$\ddot{e}_z = -s_\theta F_c/m + F_{za}(\widehat{\phi}, \widehat{\theta}, \widehat{\psi}, \alpha, \beta) + g - \ddot{z}_d + \widehat{\Delta}_z = -k_{p1}\widehat{e}_z - k_{p2}\widehat{\dot{e}}_z \tag{68}$$

Then, the desired pitch angle is

$$\theta_d = \arcsin \frac{m(F_{za}(\widehat{\phi}, \widehat{\theta}, \widehat{\psi}, \alpha, \beta) + g - \ddot{z}_d + \widehat{\Delta}_z + k_{p1}\widehat{e}_z + k_{p2}\widehat{\dot{e}}_z)}{F_c} \tag{69}$$

Also, from (56) and (65), we get

$$\begin{aligned} \ddot{e}_x &= c_\theta c_\psi F_c/m + F_{xa}(\widehat{\phi}, \widehat{\theta}, \widehat{\psi}, \alpha, \beta) + \widehat{\Delta}_x = -k_{p1}\widehat{e}_x - k_{p2}\widehat{\dot{e}}_x \\ \ddot{e}_y &= c_\theta s_\psi F_c/m + F_{ya}(\widehat{\phi}, \widehat{\theta}, \widehat{\psi}, \alpha, \beta) + \widehat{\Delta}_y = -k_{p1}\widehat{e}_y - k_{p2}\widehat{\dot{e}}_y \end{aligned} \tag{70}$$

Then, the desired yaw angle is

$$\psi_d = \arctan \frac{F_{ya}(\widehat{\phi}, \widehat{\theta}, \widehat{\psi}, \alpha, \beta) + \widehat{\Delta}_y + k_{p1}\widehat{e}_y + k_{p2}\widehat{\dot{e}}_y}{F_{xa}(\widehat{\phi}, \widehat{\theta}, \widehat{\psi}, \alpha, \beta) + \widehat{\Delta}_x + k_{p1}\widehat{e}_x + k_{p2}\widehat{\dot{e}}_x} \tag{71}$$

The combination of lift force from the wings, elevator and fuselage can provide the centripetal force. The radius of curvature is

$$r = \frac{\dot{x}^2 + \dot{y}^2}{|\dot{x}\ddot{y} - \dot{y}\ddot{x}|} \tag{72}$$

and the centripetal force is

$$f_{centri} = \frac{m(\dot{x}^2 + \dot{y}^2)}{r} = m |\dot{x}\ddot{y} - \dot{y}\ddot{x}| \tag{73}$$

Also, the centripetal force can be expressed by

$$f_{centri} = L_{wef} \cos \phi_d \tag{74}$$

where, $L_{wef} = -(L_1 + L_2)c_\alpha - (D_1 + D_2)s_\alpha - L_e c_\alpha - D_e s_\alpha - L_f c_\alpha - D_f s_\alpha$. Then, we get the desired roll angle

$$\phi_d = \arccos \frac{f_{centri}}{L_{wef}} \tag{75}$$

(5) Controller design for attitude dynamics

For attitude dynamics (54), to track the desired attitude $\Theta_d = (\psi_d, \theta_d, \phi_d)$, when we select the following controller, the attitude system error (58) will converge asymptotically to zero:

$$u_a = -\widehat{\Xi}_a - \widehat{\Delta}_a - k_{a1}\widehat{e}_a - k_{a2}\dot{\widehat{e}}_a \tag{76}$$

where, k_{a1}, k_{a2} ; $\widehat{e}_\phi = \widehat{\phi} - \phi_d, \dot{\widehat{e}}_\phi = \dot{\widehat{\phi}} - \dot{\phi}_d, \widehat{e}_\theta = \widehat{\theta} - \theta_d, \dot{\widehat{e}}_\theta = \dot{\widehat{\theta}} - \dot{\theta}_d, \widehat{e}_\psi = \widehat{\psi} - \psi_d, \dot{\widehat{e}}_\psi = \dot{\widehat{\psi}} - \dot{\psi}_d; \widehat{e}_a = [\widehat{e}_\phi \ \widehat{e}_\theta \ \widehat{e}_\psi]^T; \dot{\widehat{e}}_a = [\dot{\widehat{e}}_\phi \ \dot{\widehat{e}}_\theta \ \dot{\widehat{e}}_\psi]^T; (\widehat{\phi}, \widehat{\theta}, \widehat{\psi})$ are from the outputs of the correctors; $\widehat{\Delta}_a$ is from the outputs of the extended state observers; and

$$\widehat{\Xi}_a = \begin{bmatrix} a_\phi(\widehat{\phi}, \widehat{\theta}, \widehat{\psi}, \dot{\phi}, \dot{\theta}, \dot{\psi}, \alpha, \beta) - \ddot{\phi}_d \\ a_\theta(\widehat{\phi}, \widehat{\theta}, \widehat{\psi}, \dot{\phi}, \dot{\theta}, \dot{\psi}, \alpha, \beta) - \ddot{\theta}_d \\ a_\psi(\widehat{\phi}, \widehat{\theta}, \widehat{\psi}, \dot{\phi}, \dot{\theta}, \dot{\psi}, \alpha, \beta) - \ddot{\psi}_d \end{bmatrix} \tag{77}$$

7.0 Simulation examples

We use two examples to illustrate the sliding mode corrector presented in Theorems 5.1 and 5.2.

Example 1 (sliding mode corrector design from Theorem 5.1):

(1) Sensor outputs and actual values

Measurement signals for position and velocity: $p_m(t) = p_0(t) + d_1(t), v_m(t) = v_0(t) + d_2(t)$ where, $d_1(t)$ and $d_2(t)$ are the disturbances in position and velocity measurements, respectively; Suppose the actual position: $p_0(t) = 10 + 20 \sin(t)$; and the actual velocity: $v_0(t) = 20 \cos(t)$.

(2) Disturbance in position measurement

Position sensing disturbance $d_1(t) = d_{11}(t) + d_{12}(t)$ includes disturbance $d_{11}(t)$ and stochastic noise $d_{12}(t)$. We consider the following three types of disturbance $d_{11}(t)$:

- (a) $d_{11}(t) = 2 \sin(4t) + \cos(9t)$;
- (b) $d_{11}(t) = 6 \sin(4t) + 3 \cos(9t)$, and stochastic noise $3d_{12}(t)$ (disturbance magnitude increases, i.e. L_1 increases)
- (c) $d_{11}(t) = 1.5 \cos(0.2t) + 0.5 \sin(0.6t) + 2 \sin(4t) + \cos(9t)$ (disturbance in low and mid frequency bands)

(3) Disturbance in velocity measurement

Velocity sensing disturbance $d_2(t) = d_{21}(t) + d_{22}(t) + d_{23}(t)$ includes time-varying disturbance $d_{21}(t)$, constant disturbance $d_{22}(t)$ and stochastic noise $d_{23}(t)$. We suppose $d_{21}(t) = 0.05 \cos(0.3t) + 0.03 \sin(0.6t)$ and $d_{22}(t) = 0.02$.

(4) Determination of upper-bound of sensor accuracy ratio

From the sensor accuracy, we can get $\sup_{t \in [0, \infty)} |d_1(t)| \leq L_1 = 3$ (m), $\sup_{t \in [0, \infty)} |d_2(t)| \leq L_2 = 0.1$ (m/s). The upper-bound of sensor accuracy ratio $\varepsilon = 0.034$ can be selected such that the sensor accuracy inequality $\frac{L_2}{L_1} = \frac{0.1}{3} \leq \varepsilon = 0.034 \ll 1$ holds.

(5) Corrector parameters' selection

From the corrector parameter selection in the Remark 5.2 of Theorem 5.1, we select $r = \frac{1}{2}$ to get the minimum value and minimum range of rejection ratio $\rho(\omega_1)$: $\min \{\rho(\omega_1)\} = \frac{1}{2}\varepsilon^{\frac{1}{2}}$, and $\rho(\omega_1) \in \left(\frac{1}{2}\varepsilon^{\frac{1}{2}}, 1 + \frac{1}{2}\varepsilon^{\frac{1}{2}}\right]$ when $\omega_1 \in [0, \infty)$.

Therefore, from $\varepsilon = 0.034$ and $r = \frac{1}{2}$, we can determine the corrector parameter $k_1 = 2\varepsilon^{1-r} = 2 \times 0.034^{1-0.5} = 0.36$.

According to $\sup_{t \in [0, \infty)} |\dot{v}_0(t)| \leq L_3 = 10$, $k_2 > k_1 + L_3$ and $k_3 > L_3$, we select $k_2 = 100$, $k_3 = 100$.

(6) Rejection ratio and disturbance frequency bands

From $\varepsilon = 0.034$ and $r = \frac{1}{2}$, the rejection ratio is expressed by

$$\rho(\omega_1) = \frac{1}{\sqrt{1 + \frac{1}{4}\varepsilon^{2r-2}\omega_1^2}} + \frac{1}{2}\varepsilon^r = \frac{1}{\sqrt{1 + 7.35\omega_1^2}} + 0.09$$

and we get:

$$\begin{aligned} \omega_0 &= 4\varepsilon^{1-2r} \sqrt{1 - \frac{1}{4}\varepsilon^{2r}} = 4\sqrt{1 - \frac{1}{4} \times 0.034} = 3.98 \text{ (rad/s)} \\ \omega_c &= \frac{\varepsilon^{1-\frac{1}{2}r} \sqrt{4 - \varepsilon^r}}{1 - \frac{1}{2}\varepsilon^r} = \frac{0.034^{1-\frac{1}{4}} \sqrt{4 - 0.034^{0.5}}}{1 - \frac{1}{2} \times 0.034^{0.5}} = 0.17 \text{ (rad/s)} \end{aligned}$$

Therefore, the rejection ratio in the different frequency bands of $[0, \infty)$ can be described by:

- (i) In $[3.98\text{rad/s}, \infty)$, $\rho(\omega_1) : 0.18 \rightarrow 0.09$ as $\omega_1 : 3.98 \rightarrow \infty$ (rad/s);
- (ii) In $(0.17, 3.98\text{rad/s})$, $\rho(\omega_1) : 1 \rightarrow 0.18$ as $\omega_1 : 0.17 \rightarrow 3.98$ (rad/s);
- (iii) In $[0, 0.17\text{rad/s}]$, $\rho(\omega_1) : 1.09 \rightarrow 1$ (i.e. $\rho(\omega_1) \approx 1$) as $\omega_1 : 0 \rightarrow 0.17$ (rad/s).

Comparison with signal fusion based on Kalman filter:

We compare the sliding mode corrector with KF-based method. For this example, there are only two measurement signals, and no system model is given, we use the direct KF-based signal fusion method [25].

The position measurement is $p_m(t) = p_0(t) + d_1(t)$, and the velocity measurement is $v_m(t) = v_0(t) + d_2(t)$. According to the Taylor's expansion, position and velocity in discrete system can be expressed approximately by

$$\begin{aligned} p_0(k) &\approx p_0(k - 1) + v_0(k - 1) \cdot \Delta T \\ v_0(k) &\approx v_0(k - 1) \end{aligned} \tag{78}$$

where, ΔT is the sampling time, and k is the sample step.

Define $X(k) = [p_0(k) \ v_0(k)]^T$, $A = \begin{bmatrix} 1 & \Delta T \\ 0 & 1 \end{bmatrix}$, the above relation can be described by a matrix system:

$$X(k) = A \cdot X(k - 1) \tag{79}$$

For $p_m(t) = p_0(t) + d_1(t)$ and $v_m(t) = v_0(t) + d_2(t)$, we get

$$p_m(k) = p_0(k) + d_1(k); \ v_m(k) = v_0(k) + d_2(k) \tag{80}$$

Define $H = \begin{bmatrix} 1 & 0 \\ 0 & 1 \end{bmatrix}$, $V(k) = [d_1(k) \ d_2(k)]^T$, then the measurement outputs can be expressed by

$$Y(k) = H \cdot X(k) + V(k) \tag{81}$$

Therefore, the Kalman filter for signal integration is designed as follows:

$$\begin{aligned} X(k|k-1) &= A \cdot X(k-1|k-1) \\ P(k|k-1) &= A \cdot P(k-1|k-1)A^T + Q \\ K(k) &= \frac{P(k|k-1)H^T}{H \cdot P(k|k-1)H^T + R} \\ X(k|k) &= X(k|k-1) + K(k)(Y(k) - H \cdot X(k|k-1)) \\ P(k|k) &= (I - K(k)H)P(k|k-1) \end{aligned} \tag{82}$$

where, $I = \begin{bmatrix} 1 & 0 \\ 0 & 1 \end{bmatrix}$; $Q = \begin{bmatrix} \frac{1}{3}q_c \Delta T^3 & \frac{1}{2}q_c \Delta T^2 \\ \frac{1}{2}q_c \Delta T^2 & q_c \Delta T \end{bmatrix}$ is the process noise covariance matrix, and q_c is the power spectral density of the input white noise; and R is the measurement noise covariance matrix. In the simulation, the power spectral density of the input white noise is selected as $q_c = 1$, [25] $R = \begin{bmatrix} 0.8 & 0 \\ 0 & 0.8 \end{bmatrix}$, $P(0|0) = \begin{bmatrix} 0.1 & 0 \\ 0 & 0.1 \end{bmatrix}$ and the sampling time is $\Delta T = 0.008(\text{sec})$.

Analysis of simulation results:

The disturbance rejections in position sensing are presented in Fig. 5. Figure 5(a) describes the disturbance rejection when the disturbance $d_1(t)$ is in the frequency band that is rejected sufficiently. In fact, the frequency band of disturbance $d_1(t)$ is $\omega_1 \in [4\text{rad/s}, \infty)$, and $[4\text{rad/s}, \infty) \subset [3.98\text{rad/s}, +\infty)$. We know that in frequency band $[3.98\text{rad/s}, \infty)$, the minimum rejection ratio is obtained, i.e. $\rho(\omega_1) \in (\frac{1}{2}\varepsilon^{\frac{1}{2}}, \varepsilon^{\frac{1}{2}}) = (0.09, 0.18]$. Therefore, the position disturbance is rejected sufficiently.

Figure 5(b) presents the disturbance rejection when the magnitude of disturbance $d_1(t)$ increases. Even the position sensing accuracy becomes worse ($L_1 : 3 \text{ m} \rightarrow 9 \text{ m}$), the corrector with the original parametres can still reject the disturbance sufficiently.

Figure 5(c) shows the disturbance rejection when the position disturbance $d_1(t)$ covers the low/min/high frequency bands. In the disturbance $d_1(t)$, the mid/high frequency part is rejected sufficiently. Even the low-frequency disturbance exists, the effect of disturbance can still be rejected largely. In fact, in the position disturbance $d_1(t) = d_{11}(t) + d_{12}(t)$ (where, $d_{11}(t) = 1.5 \cos(0.2t) + 0.5 \sin(0.6t) + 2 \sin(4t) + \cos(9t)$ and the high-frequency stochastic noise $d_{12}(t)$):

- (1) the part $2 \sin(4t) + \cos(9t)$ is within the frequency band $[3.98\text{rad/s}, \infty)$, and the rejection ratio is minimum, i.e. $\rho(\omega_1) \in (0.09, 0.18]$; therefore, this part of disturbance is rejected sufficiently; $d_{12}(t)$ is also rejected sufficiently due to its high frequency.
- (2) the part $1.5 \cos(0.2t) + 0.5 \sin(0.6t)$ is within the frequency band $(0.17, 3.98\text{rad/s}]$, and the rejection ratio is $\rho(\omega_1) \in [0.18, 1\text{rad/s})$; therefore, this part of disturbance is still reduced.

From Fig. 5, we can also find that the estimate outputs of corrector are accurate and smoothed even stochastic noise exists in position and velocity measurements. In addition, if initial calibration is done for position sensing, the corrector error keeps small from the beginning; and if there is no initial calibration for position sensing, the corrector error can still converge to the small bound. The corrector performance is compared with the estimate results of the KF-based method. Comparing to the corrector, due to the existence of widely frequency-band disturbance in position sensing, the obviously large estimate errors exist in the outputs of the KF, although it can reduce the effect of disturbance to some extent.

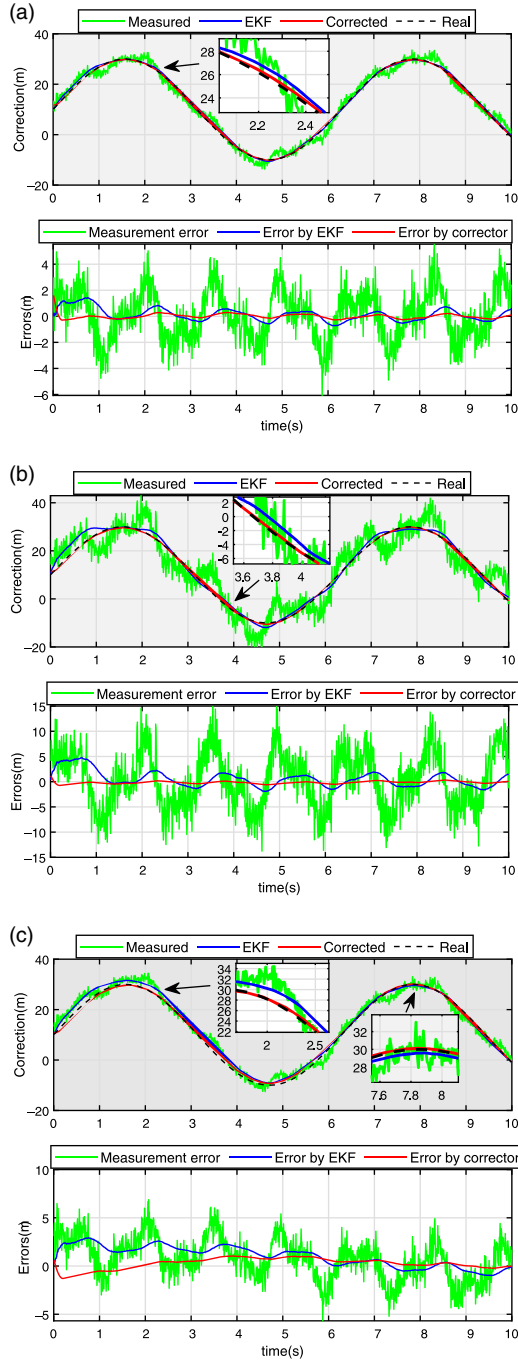


Figure 5. Example 1 – Simulation on position disturbance rejection. (a) Disturbance rejection when $L_1 = 3$. (b) Disturbance rejection when $L_1 = 9$. (c) Disturbance rejection when low-frequency disturbance is also included.

Example 2 (sliding mode corrector design from Theorem 5.2):

This example illustrates the position disturbance $d_1(t)$ is rejected to the maximum extent within a given frequency band, and the disturbance in the other bands can still be reduced largely. The corrector parameters are determined to get an optimal value of rejection ratio in the given frequency band.

(1) Sensor outputs and actual values

Sensing signals for position and velocity are $p_m(t) = p_0(t) + d_1(t)$ and $v_m(t) = v_0(t) + d_2(t)$, respectively, where, $d_1(t)$ and $d_2(t)$ are the disturbances in position and velocity sensing, respectively; the actual position: $p_0(t) = 10 + 20 \sin(t)$; and the actual velocity: $v_0(t) = 20 \cos(t)$.

(2) Disturbance in position sensing

Position sensing disturbance $d_1(t) = d_{11}(t) + d_{12}(t)$ includes time-varying disturbance $d_{11}(t)$ and stochastic noise $d_{12}(t)$, and we suppose $d_{11}(t) = 2 \sin(1.5t) + \cos(3t)$.

(3) Disturbance in velocity sensing

Velocity sensing disturbance $d_2(t) = d_{21}(t) + d_{22}(t) + d_{23}(t)$ includes time-varying disturbance $d_{21}(t)$, constant disturbance $d_{22}(t)$, and stochastic noise $d_{23}(t)$. We suppose $d_{21}(t) = 0.05 \cos(0.3t) + 0.03 \sin(0.6t)$ and $d_{22}(t) = 0.02$.

(4) Corrector parameters' selection

In this example, we suppose the disturbance $d_1(t)$ is required to be rejected sufficiently in the given frequency band $[\omega_{req}, \infty) = [1 \text{ rad/s}, \infty)$, and a small rejection ratio is obtained in this frequency band. From $\omega_{req} = 1 \text{ rad/s}$, we can get the unique solution x_{\min} to

$$1^2 x_{\min} (1 + 0.5^2 x_{\min}^2)^{-\frac{3}{2}} - 0.034 = 0$$

in the range $(\frac{1}{\sqrt{2} \times 1}, \infty)$, i.e. $x_{\min} = 5.26$, and $k_1 = 1/x_{\min} = 0.19$.

According to $\sup_{t \in [0, \infty)} |\dot{v}_0(t)| \leq L_3 = 20$, $k_2 > k_1 + L_3$ and $k_3 > L_3$, we select $k_2 = 100$, $k_3 = 100$.

(5) Rejection ratio and disturbance frequency bands

From the sensor accuracy $L_1 = 3 \text{ (m)}$ and $L_2 = 0.1 \text{ (m/s)}$, the upper-bound of sensor accuracy ratio $\varepsilon = 0.034$ is selected such that the sensor accuracy inequality $\frac{L_2}{L_1} = \frac{0.1}{3} \leq \varepsilon = 0.034 \ll 1$ holds.

From $\varepsilon = 0.034$ and $x_{\min} = 5.26$, the rejection ratio can be expressed by

$$\rho(\omega_1) = \frac{1}{\sqrt{1 + x_{\min}^2 \omega_1^2}} + \varepsilon \cdot x_{\min} = \frac{1}{\sqrt{1 + 27.67 \omega_1^2}} + 0.18$$

Therefore, the rejection ratio in the different frequency bands of $[0, \infty)$ can be described by:

- (i) In $[1 \text{ rad/s}, \infty)$, $\rho(\omega_1) : 0.37 \rightarrow 0.18$ as $\omega_1 : 1 \rightarrow \infty \text{ (rad/s)}$;
- (ii) In $(0.13, 1 \text{ rad/s})$, $\rho(\omega_1) : 1 \rightarrow 0.37$ as $\omega_1 : 0.13 \rightarrow 1 \text{ (rad/s)}$, in which, $\omega_c = \frac{\sqrt{\frac{2\varepsilon}{x_{\min}} \sqrt{1 - \frac{1}{2} \varepsilon x_{\min}}}}{1 - \varepsilon x_{\min}} = 0.13 \text{ (rad/s)}$;
- (iii) In $[0, 0.13 \text{ rad/s}]$, $\rho(\omega_1) : 1.18 \rightarrow 1$ as $\omega_1 : 0 \rightarrow 0.13 \text{ (rad/s)}$.

The disturbance rejection for Example 2 is presented in Fig. 6. Due to the relatively small rejection ratio $\rho(\omega_1) \in (0.18, 0.37]$ when $\omega_1 \in [1 \text{ rad/s}, \infty)$, the disturbance $d_1(t)$ in position sensing is rejected sufficiently in the given frequency band $[1 \text{ rad/s}, \infty)$. Also, we can find that the corrector has strong

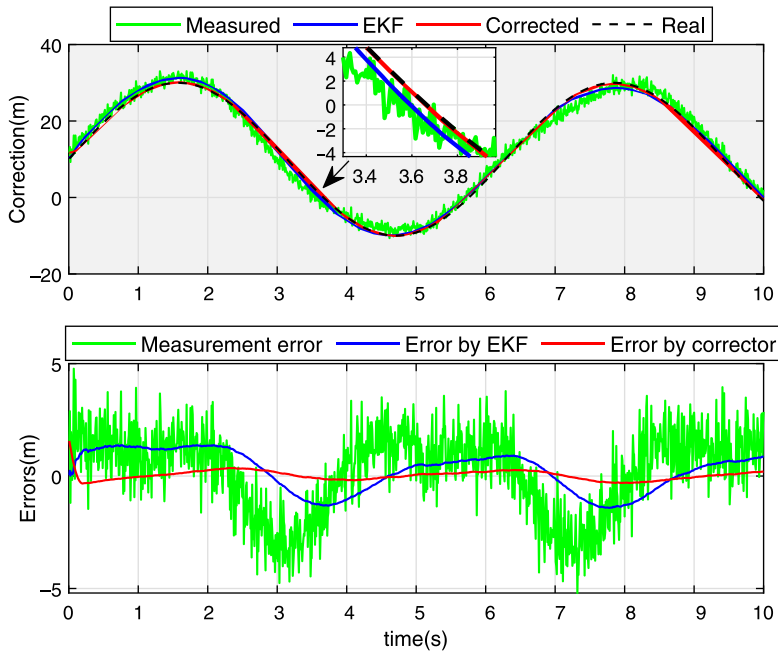


Figure 6. Example 2 – Simulation on position disturbance rejection for the given frequency band.

robustness against stochastic noise from the measurements of position and velocity, and the estimate output is smoothed. Thus, the plot performance confirms the results of numerical calculation.

For example 1, when $\omega_1 = 1$ rad/s, we can get $\rho(\omega_1) = \frac{1}{\sqrt{1+7.35\omega_1^2}} + 0.09 = 0.44$ rad/s. Therefore, in the given frequency band $[1 \text{ rad/s}, \infty)$, the rejection ratio $\rho(\omega_1)$ it satisfies $\rho(\omega_1) : 0.44 \rightarrow 0.09$ as $\omega_1 : 1 \rightarrow \infty$ (rad/s). The rejection performance of Example 1 is a little worse than that of Example 2 near the frequency ω_1 due to $0.44 > 0.37$. However, in low frequency band, the method in Example 1 can get better performance because $\rho(\omega_1) : 1.09 \rightarrow 1$ (i.e. $\rho(\omega_1) \approx 1$) as $\omega_1 : 0 \rightarrow 0.17$ (rad/s); while, for Example 2, we can get $\rho(\omega_1) : 1.18 \rightarrow 1$ as $\omega_1 : 0 \rightarrow 0.13$ (rad/s). For the whole frequency range $[0, \infty)$, the corrector in Example 1 can get $\rho(\omega_1) : 1.09 \rightarrow 0.09$ as $\omega_1 : 0 \rightarrow \infty$, while the corrector in Example 2 can get $\rho(\omega_1) : 1.18 \rightarrow 0.18$ as $\omega_1 : 0 \rightarrow \infty$.

8.0 Experiment on jet UAV navigation and control

In this section, an experiment on a jet UAV flight is presented. The jet UAV prototype (an RC-model-based F/A-18 Hornet) shown in Fig. 2 is used for the flight test [17]. A JetCat P200-SX jet engine is adopted to provide the thrust, and the engine starter includes: Jet-tronic ECU for fuel control; electronic valve; electronic starting gas valve; electronic fuel valve; fuel tubing, tubing connector set, filters and cable set; 2-cell, 3,300mA LiPoly battery pack; and starting gas tank. The engine can provide 220N (52 lbs) thrust for 112,000 RPM, and RPM range: 33000 ~ 112000 RPM. A Gumstix microcomputer is used for data collection and signal processing from sensors. The flight control system implementation on the hardware is shown in Fig. 7. An Arduino Mega 2560 is taken as the driver board, which has multiple PWM output channels. The input voltage is 7 ~ 12 V. The control update time is 5ms. The FUTABA S3001 servos are adopted to control the deflections of ailerons, elevators and rudders. A 10Hz GPS MediaTek MT3329 is selected as the GPS receiver. A 9Hz VTI SCP1000 altimetre with 10cm resolution is utilised for above the sea level altitude measurements at higher altitudes. A 12Hz SF02-F laser altimetre is used for altitude measurements at lower altitudes with 40m range. A 10kHz

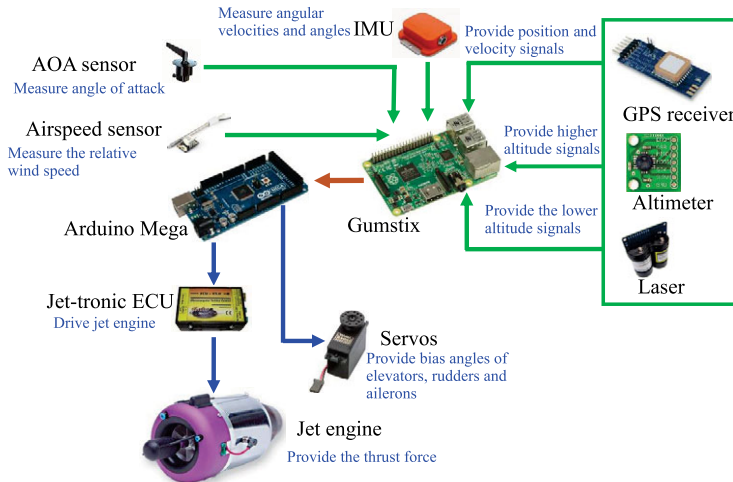


Figure 7. Control system hardware.

Xsens MTI AHRS provides the 3-axial accelerations, the angular rates and the earth’s magnetic field. A 192kHz kpitot 32 digital air speed sensor is utilised to obtain the relative wind speed. A 100kHz 4239-01 AOA sensor is used to measure the angle-of-attack.

The jet UAV parametres are described in Table 1.

Measurements of position and velocity: A 10Hz GPS MediaTek MT3329 (without aid) provides position at accuracy of 3m and velocity at accuracy of 0.1m/s.

Measurements of attitude angle and angular velocity: A 10kHz Xsens MTI AHRS provides attitude angles and angular velocity, in which: roll/pitch accuracy: 0.5°, yaw accuracy: 1.0°; angular accuracy: 9°/hr = 0.0025°/s.

Desired flight trajectory: The desired flight trajectory consists of takeoff, climb, cruise in a circle with the radius 500m and the height 300 m, and landing back, which is shown in Fig. 8(a).

In the experiment, considering measurement disturbances and the uncertainties in the UAV flight dynamics, the jet UAV is controlled to track the reference trajectory. The position and velocity are obtained from the GPS receiver, and the attitude angle and the angular velocity are measured by the IMU. The corrected positions from the correctors and the system uncertainty estimations from the extended state observers are used for determination of the desired attitude and design of the controllers. The controllers (65) and (76) drive the UAV to track the reference trajectory. The performance of position correction by the correctors is compared with the EKF-based method [21].

8.1 Design of correctors

8.1.1 Determination of upper-bound of sensor accuracy ratio

From the position sensor accuracy, we get $\sup_{t \in [0, \infty)} |d_{*1}(t)| \leq L_{*1} = 3$ (m), $\sup_{t \in [0, \infty)} |d_{*2}(t)| \leq L_{*2} = 0.1$ (m/s), where, $* = \{x, y, z\}$. The upper-bound of sensor accuracy ratio $\varepsilon = 0.034$ can be selected such that the sensor accuracy inequality $\frac{L_2}{L_1} = \frac{0.1}{3} \leq \varepsilon_* = 0.034 \ll 1$ holds.

From the attitude sensor accuracy, we get $\sup_{t \in [0, \infty)} |d_{*1}(t)| \leq L_{*1} = 0.5^\circ$, $\sup_{t \in [0, \infty)} |d_{*2}(t)| \leq L_{*2} = 0.0025^\circ/\text{s}$, where, $* = \{\phi, \theta\}$; and $\sup_{t \in [0, \infty)} |d_{\psi 1}(t)| \leq L_{\psi 1} = 1^\circ$, $\sup_{t \in [0, \infty)} |d_{\psi 2}(t)| \leq L_{\psi 2} = 0.0025^\circ/\text{s}$. For the roll/pitch, the upper-bound of sensor accuracy ratio $\varepsilon_* = 0.005$ can be selected such that the sensor accuracy inequality $\frac{L_2}{L_1} = \frac{0.0025}{0.5} \leq \varepsilon_* = 0.005 \ll 1$ holds, where, $* = \{\phi, \theta\}$. For the yaw, the upper-bound of sensor accuracy ratio $\varepsilon_\psi = 0.0025$ can be selected such that the sensor accuracy inequality $\frac{L_2}{L_1} = \frac{0.0025}{1} \leq \varepsilon_\psi = 0.0025 \ll 1$ holds.

Table 1. UAV parameters

Symbol	Quantity	Value
m_d	Dry weight of UAV	22.5kg
g	Gravity of acceleration	9.8m/s ²
ρ	Air density	1.225 kg/m ³
l_w	Wingspan	1.92m
S_w	Fixed wing area	1.58 m ²
$C_{L1,20}$	Fixed wing lift coefficient ($\alpha = 0$)	0.3145
$C_{D1,20}$	Fixed wing drag coefficient ($\alpha = 0$)	0.1634
$C_{L1,2\alpha}$	Fixed wing lift coefficient due to α	0.5122
$C_{L\delta1,2}$	Fixed wing lift coefficient due to δ_i	0.1634
$C_{D\delta1,2}$	Fixed wing drag coefficient due to δ_i	0.0025
A_w	Fixed wing aspect ratio	2.67
l_f	Fuselage length	2.35m
S_f	Fuselage equivalent area	0.69 m ²
$C_{lf\alpha}$	Fuselage lift coefficient due to α	0.1573
C_{df0}	Fuselage drag coefficient ($\alpha = 0$)	0.0096
$C_{df\alpha}$	Fuselage drag coefficient due to α	0.0152
S_e	Elevator area	0.36 m ²
$C_{le\alpha}$	Elevator lift coefficient due to α	0.6103
C_{de0}	Elevator drag coefficient ($\alpha = 0$)	0.0046
A_e	Elevator aspect ratio	1.15
S_r	Rudder area	0.38 m ²
$C_{lr\beta}$	Rudder force coefficient due to β	0.3261
$C_{lr\delta_r}$	Rudder lift coefficient due to δ_r	0.0075
C_{dr0}	Rudder drag coefficient ($\beta = \delta_r = 0$)	0.0046
A_r	Rudder aspect ratio	1.56
J_x	Moment inertia about axis E_x^b	18Nm
J_y	Moment inertia about axis E_y^b	18Nm
J_z	Moment inertia about axis E_z^b	34Nm

8.1.2 Corrector parameters selection

For the position, we select $r = \frac{1}{2}$ to get the minimum value and minimum range of rejection ratio $\rho(\omega_1)$: $\min\{\rho(\omega_{*1})\} = \frac{1}{2}\varepsilon_*^{\frac{1}{2}} = \frac{1}{2}0.034^{0.5} = 0.09$, and $\rho(\omega_{*1}) \in \left(\frac{1}{2}\varepsilon_*^{\frac{1}{2}}, 1 + \frac{1}{2}\varepsilon_*^{\frac{1}{2}}\right] = (0.09, 1.09]$ when $\omega_{*1} \in [0, +\infty)$, where, $*$ = {x, y, z}.

From $\varepsilon_* = 0.034$ and $r = \frac{1}{2}$, we can determine the corrector parameter $k_{*1} = 2\varepsilon_*^{1-r} = 2 \times 0.034^{1-0.5} = 0.36$.

According to $\sup_{t \in (0, \infty)} |\dot{y}_{*0}(t)| \leq L_{*3} = 50$, $k_{*2} > k_{*1} + L_{*3}$ and $k_{*3} > L_{*3}$, we select $k_{*2} = 100$, $k_{*3} = 100$, where, $*$ = {x, y, z}.

For the attitude, we know that $\varepsilon_\phi = 0.005$, $\varepsilon_\theta = 0.005$ and $\varepsilon_\psi = 0.0025$, we select $r = \frac{1}{2}$. Then, we get the minimum rejection ratio $\min\{\rho(\omega_{*1})\} = \frac{1}{2}\varepsilon_*^{\frac{1}{2}} = \frac{1}{2}0.005^{0.5} = 0.035$, and $\rho(\omega_{*1}) \in (0.035, 1.035]$ when $\omega_{*1} \in [0, \infty)$, where, $*$ = { ϕ , θ }; and $\min\{\rho(\omega_{\psi 1})\} = \frac{1}{2}\varepsilon_{\psi}^{\frac{1}{2}} = \frac{1}{2}0.0025^{0.5} = 0.025$, and $\rho(\omega_{\psi 1}) \in (0.025, 1.025]$ when $\omega_{\psi 1} \in [0, \infty)$.

Therefore:

From $\varepsilon_* = 0.005$ and $r = \frac{1}{2}$, we can determine $k_{*1} = 2\varepsilon_*^{1-r} = 2 \times 0.005^{1-0.5} = 0.14$, where, $*$ = { ϕ , θ }.

From $\varepsilon_\psi = 0.0025$ and $r = \frac{1}{2}$, we can determine $k_{\psi 1} = 2\varepsilon_\psi^{1-r} = 2 \times 0.0025^{1-0.5} = 0.1$.

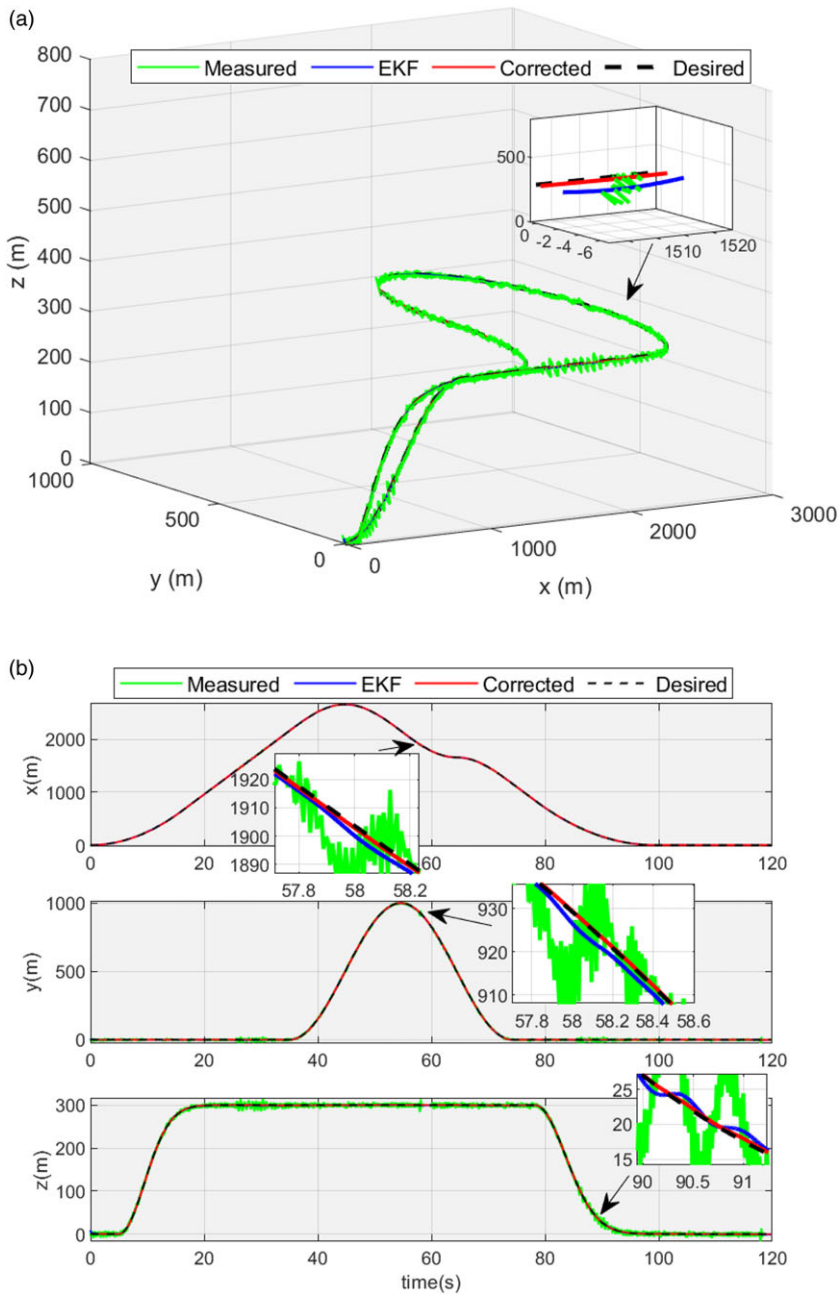


Figure 8. UAV flight based on correction. (a) 3D navigation trajectories. (b) Position comparison in the three directions.

For the other parameters, to overcome the effect of angular accelerations on the correctors, we select the relatively large $k_{\ast 2} = 10, k_{\ast 3} = 10$, where, $\ast = \{\phi, \theta, \psi\}$.

Therefore, we get the corrector parameters.

Correctors for position: $k_{\ast 1} = 0.36, k_{\ast 2} = 100, k_{\ast 3} = 100$, where, $\ast = \{x, y, z\}$;

Correctors for attitude: $k_{\phi 1} = 0.14, k_{\theta 1} = 0.14, k_{\psi 1} = 0.1; k_{\ast 2} = 10, k_{\ast 3} = 10$, where, $\ast = \{\phi, \theta, \psi\}$.

8.1.3 Rejection ratio and disturbance frequency bands

(1) Rejection ratios in the disturbance frequency bands for position

From $\varepsilon_* = 0.034$ and $r = \frac{1}{2}$, where, $*$ = {x, y, z}, the rejection ratio is expressed by

$$\rho(\omega_{*1}) = \frac{1}{\sqrt{1 + \frac{1}{4}\varepsilon_*^{2r-2}\omega_{*1}^2}} + \frac{1}{2}\varepsilon_*^r = \frac{1}{\sqrt{1 + 7.35\omega_{*1}^2}} + 0.09$$

Therefore, the rejection ratios in the different frequency bands of $[0, +\infty)$ can be described by:

- (i) In $[3.98\text{rad/s}, \infty)$, $\rho(\omega_{*1}) : 0.18 \rightarrow 0.09$ as $\omega_{*1} : 3.98 \rightarrow \infty$ (rad/s);
- (ii) In $(0.17, 3.98\text{rad/s})$, $\rho(\omega_{*1}) : 1 \rightarrow 0.18$ as $\omega_{*1} : 0.17 \rightarrow 3.98$ (rad/s);
- (iii) In $[0, 0.17\text{rad/s}]$, $\rho(\omega_{*1}) : 1.09 \rightarrow 1$ (i.e. $\rho(\omega_{*1}) \approx 1$) as $\omega_{*1} : 0 \rightarrow 0.17$ (rad/s).

(2) Rejection ratios in the disturbance frequency bands for attitude (ϕ, θ)

From $\varepsilon_* = 0.005$ and $r = \frac{1}{2}$, where, $*$ = { ϕ, θ }, the rejection ratio is expressed by

$$\rho(\omega_{*1}) = \frac{1}{\sqrt{1 + \frac{1}{4}\varepsilon_*^{2r-2}\omega_{*1}^2}} + \frac{1}{2}\varepsilon_*^r = \frac{1}{\sqrt{1 + 50\omega_{*1}^2}} + 0.035$$

Therefore, the rejection ratios in the different frequency bands can be described by:

- (i) In $[4\text{rad/s}, \infty)$, $\rho(\omega_{*1}) : 0.07 \rightarrow 0.035$ as $\omega_{*1} : 4 \rightarrow \infty$ (rad/s);
- (ii) In $(0.04, 4\text{rad/s})$, $\rho(\omega_{*1}) : 1 \rightarrow 0.07$ as $\omega_{*1} : 0.04 \rightarrow 4$ (rad/s);
- (iii) In $[0, 0.04\text{rad/s}]$ $\rho(\omega_{*1}) : 1.035 \rightarrow 1$ (i.e. $\rho(\omega_{*1}) \approx 1$) as $\omega_{*1} : 0 \rightarrow 0.04$ (rad/s).

(3) Rejection ratios in the disturbance frequency bands for attitude (ψ)

From $\varepsilon_\psi = 0.0025$ and $r = \frac{1}{2}$, the rejection ratio is expressed by

$$\rho(\omega_{\psi 1}) = \frac{1}{\sqrt{1 + \frac{1}{4}\varepsilon_\psi^{2r-2}\omega_{\psi 1}^2}} + \frac{1}{2}\varepsilon_\psi^r = \frac{1}{\sqrt{1 + 100\omega_{\psi 1}^2}} + 0.025$$

Therefore, the rejection ratios in the different frequency bands can be described by:

- (i) In $[4\text{rad/s}, \infty)$, $\rho(\omega_{\psi 1}) : 0.05 \rightarrow 0.025$ as $\omega_{\psi 1} : 4 \rightarrow \infty$ (rad/s);
- (ii) In $(0.023, 4\text{rad/s})$, $\rho(\omega_{\psi 1}) : 1 \rightarrow 0.05$ as $\omega_{\psi 1} : 0.023 \rightarrow 4$ (rad/s);
- (iii) In $[0, 0.023\text{rad/s}]$, $\rho(\omega_{\psi 1}) : 1.025 \rightarrow 1$ (i.e. $\rho(\omega_{\psi 1}) \approx 1$) as $\omega_{\psi 1} : 0 \rightarrow 0.023$ (rad/s).

8.2 Parametres of observers and controllers

According to the selection rules of observer parametres [24], we select the extended state observer parametres: $\lambda_{1*} = 4$, $\lambda_{*2} = 20$, $\alpha_* = 0.6$, where, $*$ = {x, y, z, θ, ϕ, ψ }. According to the properties and tests of engine and digital servos, we select the control law parametres: $k_{p1} = 16$, $k_{p2} = 8$, $k_{a1} = 25$, $k_{a2} = 8$.

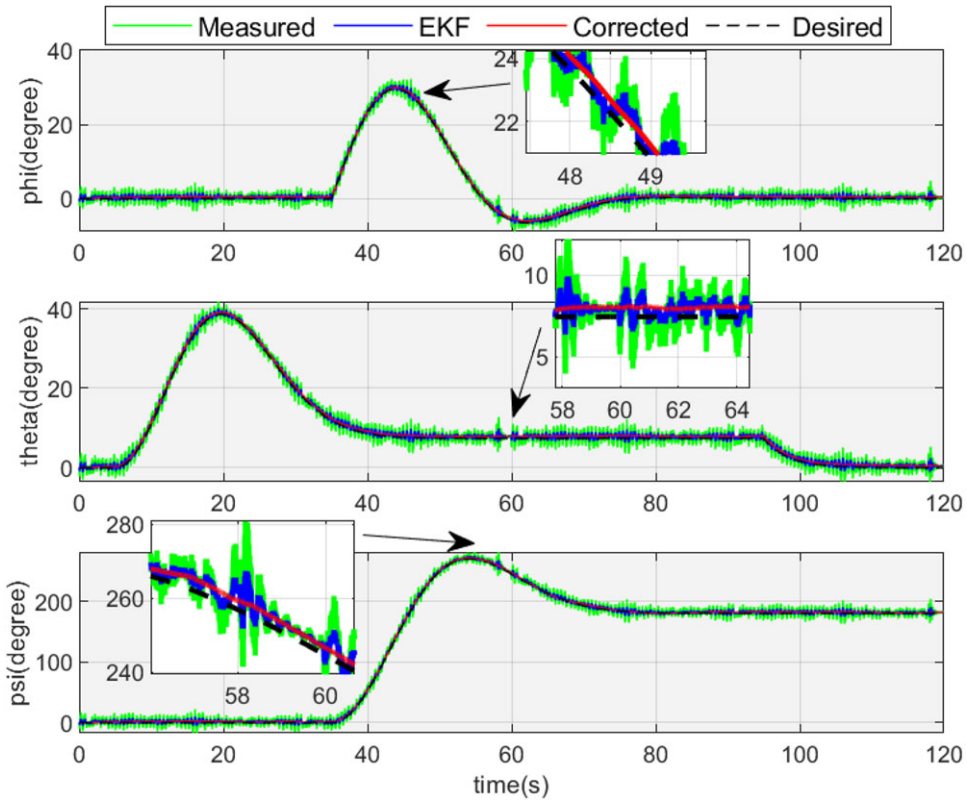


Figure 9. Attitude correction.

8.3 Analysis of UAV navigation and control performance

Figure 8(a) shows the comparison of the flight trajectories, including the measured from GPS, the reference trajectory, and the estimations by the corrector and the EKF-based method. Meanwhile, the trajectory comparisons in the three directions are shown in Fig. 8(b): due to the effect of adverse conditions, e.g. engine vibration and communication, the actual measurement disturbances in position from GPS were about 10m. The estimate errors by the corrector were less than 1m, while the estimate errors by the KF were about 3m. From the estimate errors and the above numerical calculation, we can find that the position disturbances were mainly within the frequency band $[3.98\text{rad/s}, +\infty)$. Therefore, the disturbances in position measurements were rejected sufficiently by the correctors, and the correctors provided the relatively accurate and smoothed correction outputs. The attitude angle comparisons in the three directions are shown in Fig. 9. During the UAV flight, the actual measurement disturbances in attitude from the IMU were about $3^\circ \sim 4^\circ$. The corrector estimate errors for attitude angle were less than 0.2° . Then, comparing the above calculation, we can find that the attitude disturbances were mainly within the frequency band $[4\text{rad/s}, +\infty)$. Therefore, the disturbances in the attitude measurements were rejected sufficiently by the correctors due to the very small rejection ratio in this frequency band. From the flight test, we can find that the correctors also reduced the sensing disturbances from the effect of UAV vibrations, and the jet UAV remained in the safe flight condition throughout the flight.

9.0 Conclusions

In this paper, a sliding mode corrector has been presented, which can correct disturbance in position measurement using relatively accurate velocity. The performance of the corrector was demonstrated

by two simulation examples and a jet UAV flight test: (i) it succeeded in rejecting the disturbances largely in position and attitude sensing, even though the disturbances are in the low/mid/high frequency bands; (ii) the experimental test verified the validity of the corrector's providing accurate and smoothed estimate of position and attitude; (iii) the estimate outputs from the correctors can be used directly by the control system without any additional filters. The merits of the corrector include its model free, bounded corrector gains, the accurate and smoothed estimate outputs and strong parameter inclusion to change of disturbance and signal.

References

1. Panagiotou, P. and Yakinthos, K. Aerodynamic efficiency and performance enhancement of fixed-wing UAVs. *Aerosp Sci Technol*, 2020, **99**, pp 105575.
2. Footohi, P., Bouskela, A. and Shkarayev, S.V. Aerodynamic design of long-range VTOL UAV. In *AIAA Scitech 2019 Forum*, 7-11 Jan., San Diego, CA, 2019, pp 2291.
3. Yan, Y., Yang, J., Liu, C., Coombes, M., Li, S. and Chen, W.H. On the actuator dynamics of dynamic control allocation for a small fixed-wing UAV with direct lift control. *IEEE Trans Control Syst Technol*, 2020, **28**, (3), pp 984–991.
4. Adami, T.M. and Zhu, J.J. 6DOF flight control of fixed-wing aircraft by trajectory linearization. In *Proceedings of the 2011 American Control Conference*, 29 Jun-01 Jul., San Francisco, CA, 2011, pp 1610–1617.
5. Hsu, L.T. Analysis and modeling GPS NLOS effect in highly urbanized area, *GPS Solut*, 2018, **22**, (7), pp 1–12.
6. Abdel-Hafez, M.F. Detection of bias in GPS satellites' measurements: A probability ratio test formulation. *IEEE Trans Control Syst Technol*, 2014, **22**, (3), pp 1166–1173.
7. Freda, P., Angrisano, A., Gaglione, S. and Troisi, S. Time differenced carrier phases technique for precise GNSS velocity estimation. *GPS Solut*, 2015, **19**, pp 335–341.
8. Serrano, L., Kim, D., Langley, R.B., Itani, K. and Ueno, M. A GPS velocity sensor: How accurate can it be? – A first look, *ION NTM 2004*, 26-28 Jan., San Diego, CA, 2004, pp 875–885.
9. Rahman, A., Lubecke, V.M., Boric-Lubecke, O., Prins, J.H. and Sakamoto, T. Doppler radar techniques for accurate respiration characterization and subject identification. *IEEE J Emerg Sel Topics Circuits Syst*, 2018, **8**, (2), pp 350–359.
10. Levant, A. High-order sliding modes, differentiation and outputfeedback control, *Int J Control*, 2003, **76**, (9/10), pp 924–941.
11. Khalil, H.K. Cascade high-gain observers in output feedback control, *Automatica*, 2017, **80**, pp 110–118.
12. Rogne, R.H., Bryne, T.H., Fossen, T.I. and Johansen, T.A. On the usage of low-cost mems sensors, strapdown inertial navigation, and nonlinear estimation techniques in dynamic positioning. *IEEE J Ocean Eng*, 2020, **46**, (1), pp 24–39.
13. Wang, X., Shirinzadeh, B. and Ang Jr, M.H. Nonlinear double-integral observer and application to quadrotor aircraft, *IEEE Trans Ind Electron*, 2015, **62**, (2), pp 1189–1200.
14. Ludwig, S.A. and Jiménez, A.R. Optimization of gyroscope and accelerometer/magnetometer portion of basic attitude and heading reference system, 2018 *IEEE International Symposium on Inertial Sensors and Systems (INERTIAL)*, Moltrasio, Italy, 26-29 Mar., 2018, pp 1–4.
15. Lin, C.L., Hsieh, S.L. and Lin, Y.P. Trajectory estimation based on extended state observer with Fal-filter. *Aeronaut J*, 2015, **119**, (1218), pp.1017–1031.
16. Panchal, B., Subramanian, K. and Talole, S.E. Robust missile autopilot design using two time-scale separation. *IEEE Trans Aerosp Electron Syst*, 2018, **54**, (3), pp 1499–1510.
17. Wang, X. and Cai, L. Navigation and control based on integral-uncertainty observer for unmanned jet aircraft. *IEEE Trans Aerosp Electron Syst*, 2017, **53**, (3), pp 1230–1249.
18. Deo, V.A., Silvestre, F. and Morales, M. Flight performance monitoring with optimal filtering applications. *Aeronaut J*, 2020, **124**, (1272), pp 170–188.
19. Crassidis, J.L. Introduction to the special issue on the Kalman filter and its aerospace applications. *J Guid Control Dyn*, 2017, **40**, (9), pp. 2137–2137.
20. Lin, C.L., Li, J.C., Chiu, C.L., Wu, Y.W. and Jan, Y.W. Gyro-stellar inertial attitude estimation for satellite with high motion rate. *Aeronaut J*, 2022, pp 1–15.
21. Idkhajine, L., Monmasson, E. and Maalouf, A. Fully FPGA-based sensorless control for synchronous AC drive using an extended Kalman filter, *IEEE Trans Ind Electron*, 2012, **59**, (10), pp 3908–3918.
22. Wang, X. Signal corrector and decoupling estimations for UAV control, *Aeronaut J*, 2022, doi: [10.1017/aer.2022.86](https://doi.org/10.1017/aer.2022.86)
23. Çetinsoy, E., Dikyar, S., Hançer, C., Oner, K.T., Sirimoglu, E., Unel, M. and Aksit, M.F. Design and construction of a novel quad tilt-wing UAV. *Mechatronics*, 2012, **22**, (6), pp 723–745.
24. Wang, X. and Lin, H. Design and frequency analysis of continuous finite-time-convergent differentiator. *Aerosp Sci Technol*, 2012, **18**, (1), pp 69–78.
25. Tsang, C.C., Chow, G.C.T., Leong, P.H., Zhang, G., Luo, Y., Dong, Z., Shi, G., Kwok, S.Y., Wong, H.Y., Li, W.J. and Wong, M.Y. A novel real-time error compensation methodology for μ IMU-based digital writing instrument. 2006 *IEEE International Conference on Robotics and Biomimetics*, 2006, pp 678–681.
26. Perruquetti, W. and Barbot, J.P. eds. *Sliding Mode Control in Engineering*. New York: Marcel Dekker, 2002.
27. Levant, A. Sliding order and sliding accuracy in sliding mode control. *Int J Control*, 1993, **58**, (6), pp 1247–1263.

28. Boelens, O.J. CFD analysis of the flow around the X-31 aircraft at high angle of attack, *Aerosp Sci Technol*, 2012, **20**, (1), pp 38–51.
 29. Wang, X., Chen, Z. and Yuan, Z. Modeling and control of an agile tail-sitter aircraft, *J Frank Inst*, 2015, **352**, pp 5437–5472.

Appendix

Proof of Theorem 4.1

If $|e_2| > 1$, from the convergence law $\dot{e}_2 = -e_2$ or $\dot{e}_2 = -k_3 \text{sign}(e_2)$, we can get $|e_2| \leq 1$.

Select the Lyapunov function candidate as

$$V = \frac{1}{2}(e_2 + k_1 e_1)^2 \tag{83}$$

Then, if $|e_2| \leq 1$, taking the derivative of V , we get

$$\begin{aligned} \dot{V} &= (e_2 + k_1 e_1) \{-k_2 \text{sign}(e_2 + k_1 e_1) + k_1 e_2\} \\ &= -k_2 |e_2 + k_1 e_1| + k_1 e_2 (e_2 + k_1 e_1) \\ &\leq -k_2 |e_2 + k_1 e_1| + k_1 |e_2| |e_2 + k_1 e_1| \\ &\leq -(k_2 - k_1) |e_2 + k_1 e_1| \\ &= -\sqrt{2} (k_2 - k_1) V^{\frac{1}{2}} \end{aligned} \tag{84}$$

We know that $k_2 > k_1 > 0$. Therefore, there exists a time t_s , for $t \geq t_s$, such that $V = 0$, i.e. the sliding variables are on the sliding surface $e_2 + k_1 e_1 = 0$. Then, from the relation $\dot{e}_1 = e_2$, we get the following convergence law:

$$\dot{e}_1 = -k_1 e_1 \tag{85}$$

Therefore, $\lim_{t \rightarrow \infty} e_1 = 0$. Furthermore, from $\dot{e}_2 = -k_2 \text{sign}(e_2 + k_1 e_1)$, we get $\lim_{t \rightarrow \infty} e_2 = 0$. This concludes the proof. ■

Proof of Theorem 4.2

Determination of e_2 range

For (10), when $|e_2 - d_2(t)| > 1$, we get

$$\dot{e}_2 = -k_3 \text{sign}(e_2 - d_2(t)) - d_3(t) \tag{86}$$

Then, it achieves a differential inclusion

$$\dot{e}_2 \in -k_3 \text{sign}(e_2 - d_2(t)) + [-L_3, L_3] \tag{87}$$

From Lemma 8 in [10] and $k_3 > L_3$, there exists a finite time t_s , for $t \geq t_s$, such that

$$|e_2| \leq L_2 \tag{88}$$

where, $\sup_{t \in [0, \infty)} |d_2(t)| \leq L_2$. Then, there exists a time $t_s > 0$, for $t \geq t_s$, we get

$$|e_2 - d_2(t)| \leq |e_2| + |d_2(t)| \leq 2L_2 \tag{89}$$

Therefore, due to $L_2 \ll 1$, the inequality $|e_2 - d_2(t)| \leq 1$ holds for $t \geq t_s$. Then, for system (10), according to the 2-sliding mode system (8b) in Theorem 4.1 and $k_2 > k_1 + L_4$, the sliding variables e_1 and e_2 are on the sliding surface $e_2 - d_2(t) + k_1(e_1 - d_1(t)) = 0$, i.e. we get the following convergence law:

$$\dot{e}_1 = -k_1 e_1 + k_1 d_1(t) + d_2(t) \tag{90}$$

Defining the Laplace transforms $E_1(s) = L[e_1]$, $D_1(s) = L[d_1(t)]$ and $D_2(s) = L[d_2(t)]$, we get

$$sE_1(s) = -k_1 E_1(s) + k_1 D_1(s) + D_2(s) \tag{91}$$

Therefore, the error variable e_1 is expressed by

$$E_1(s) = \frac{k_1}{s + k_1} D_1(s) + \frac{1}{s + k_1} D_2(s) \tag{92}$$

For the disturbance $d_1(t)$, the transfer function $\frac{k_1}{s+k_1}$ can be taken as a filter, the disturbance $d_1(t)$ is the input and $e_1(t)$ is the output. The selection of k_1 should try to reduce the effect of $d_1(t)$ by considering the effect of disturbance $d_2(t)$ from the velocity measurement.

Suppose the disturbance $d_2(t)$ includes time varying part $d_{21}(t)$ and constant part d_{22} , i.e. $d_2(t) = d_{21}(t) + d_{22}$; the angular frequency variable of $d_{21}(t)$ is supposed to be ω_2 . We define $\sup_{t \in [0, \infty)} |d_{21}(t)| \leq L_{21} < \infty$, $\sup_{t \in [0, \infty)} |d_{22}(t)| \leq L_{22} < \infty$, and $L_2 = L_{21} + L_{22} \ll 1$.

Taking Laplace transform for $d_2(t)$, we get $D_2(s) = D_{21}(s) + \frac{d_{22}}{s}$, where, $D_2(s) = L[d_2(t)]$ and $D_{21}(s) = L[d_{21}(t)]$. Then, (92) can be expressed by

$$\begin{aligned} E_1(s) &= \frac{k_1}{s+k_1} D_1(s) + \frac{1}{s+k_1} (D_{21}(s) + \frac{d_{22}}{s}) \\ &= \frac{k_1}{s+k_1} D_1(s) + \frac{k_1}{s+k_1} \frac{D_{21}(s)}{k_1} + \frac{d_{22}}{s(s+k_1)} \end{aligned} \tag{93}$$

Boundness of corrector estimate error

Define $d_1(t) = U_1 \sin(\omega_1 t)$ and $d_{21}(t) = U_{21} \sin(\omega_2 t)$. For (93), from the frequency analysis of first-order filter, we can get

$$\lim_{t \rightarrow \infty} e_1 = \frac{U_1}{\sqrt{1 + \left(\frac{\omega_1}{k_1}\right)^2}} \sin(\omega_1 t + \phi_1) + \frac{U_{21}/k_1}{\sqrt{1 + \left(\frac{\omega_2}{k_1}\right)^2}} \sin(\omega_2 t + \phi_2) + \frac{d_{22}}{k_1} \tag{94}$$

where, $\phi_1 = -\tan^{-1} \frac{\omega_1}{k_1}$ and $\phi_2 = -\tan^{-1} \frac{\omega_2}{k_1}$. We know that $U_1 \leq L_1$, $U_{21} \leq L_{21}$ and $|d_{22}| \leq L_{22}$. Therefore, for (94), we get

$$\lim_{t \rightarrow \infty} |e_1| \leq \frac{L_1}{\sqrt{1 + \left(\frac{\omega_1}{k_1}\right)^2}} + \frac{L_{21}/k_1}{\sqrt{1 + \left(\frac{\omega_2}{k_1}\right)^2}} + \frac{L_{22}}{k_1} \tag{95}$$

Define $x = \frac{1}{k_1}$. Then, (95) can be rewritten by

$$\lim_{t \rightarrow \infty} |e_1| \leq \left(\frac{1}{\sqrt{1 + \omega_1^2 x^2}} + \frac{\frac{L_{21}}{L_1} x}{\sqrt{1 + \omega_2^2 x^2}} + \frac{L_{22}}{L_1} x \right) L_1 \tag{96}$$

In (96), for all the $\omega_2 \in [0, \infty)$, we have

$$\frac{\frac{L_{21}}{L_1} x}{\sqrt{1 + \omega_2^2 x^2}} \leq \frac{L_{21}}{L_1} x \tag{97}$$

Therefore, for (96) and $\frac{L_2}{L_1} \leq \varepsilon$, we get

$$\begin{aligned} \lim_{t \rightarrow \infty} |e_1| &\leq \left(\frac{1}{\sqrt{1 + \omega_1^2 x^2}} + \frac{L_{21} + L_{22}}{L_1} x \right) L_1 \\ &= \left(\frac{1}{\sqrt{1 + \omega_1^2 x^2}} + \frac{L_2}{L_1} x \right) L_1 \\ &= \left(\frac{1}{\sqrt{1 + \omega_1^2 x^2}} + \varepsilon \cdot x \right) L_1 \end{aligned} \tag{98}$$

Define the rejection ratio as

$$\rho(\omega_1, x) = \frac{1}{\sqrt{1 + \omega_1^2 x^2}} + \varepsilon \cdot x \tag{99}$$

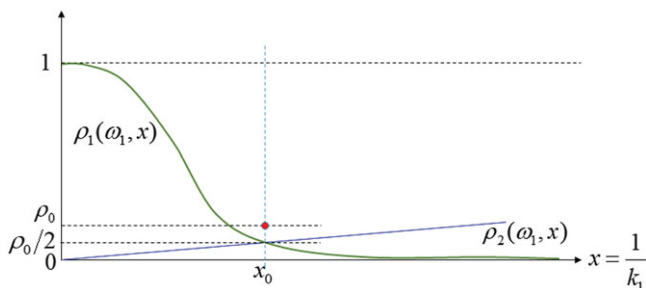


Figure 10. Rejection ratio.

Therefore, (98) can be expressed by

$$\lim_{t \rightarrow \infty} |e_1| \leq \rho(\omega_1, x)L_1 \tag{100}$$

In the rejection ratio (99), define

$$\rho_1(\omega_1, x) = \frac{1}{\sqrt{1 + \omega_1^2 x^2}}; \rho_2(\omega_1, x) = \varepsilon \cdot x \tag{101}$$

Taking the derivative for $\rho_1(\omega_1, x)$ and $\rho_2(\omega_1, x)$ about x , respectively, we get

$$\frac{d\rho_1(\omega_1, x)}{dx} = -\omega_1^2 x (1 + \omega_1^2 x^2)^{-\frac{3}{2}} < 0 \tag{102}$$

$$\frac{d\rho_2(\omega_1, x)}{dx} = \varepsilon > 0 \tag{103}$$

We know that, $\rho_1(\omega_1, x)$ is the monotonically decreasing function of x from $\rho_1(\omega_1, 0) = 1$, and $\rho_2(\omega_1, x)$ is monotonically increasing function of x from $\rho_2(\omega_1, 0) = 0$ (See $\rho_1(\omega_1, x)$ and $\rho_2(\omega_1, x)$ in Figure 10).

Therefore, $\rho_1(\omega_1, x)$ and $\rho_2(\omega_1, x)$ will intersect at a point, and we define the point $x \stackrel{\text{define}}{=} x_0$.

In the following, we consider to determine ω_1 and x to make $\rho(\omega_1, x)$ equal a given rejection ratio ρ_0 at the intersection point x_0 , i.e.

$$\rho(\omega_1, x_0) = \frac{1}{\sqrt{1 + \omega_1^2 x_0^2}} + \varepsilon \cdot x_0 = \rho_0 \tag{104}$$

and

$$\rho_1(\omega_1, x_0) = \rho_2(\omega_1, x_0) = \frac{\rho_0}{2} \tag{105}$$

holds at the the intersection point x_0 . From (104) and (105), we have

$$\begin{aligned} \frac{1}{\sqrt{1 + \omega_1^2 x_0^2}} &= \frac{\rho_0}{2} \\ \varepsilon \cdot x_0 &= \frac{\rho_0}{2} \end{aligned} \tag{106}$$

Solving the equations in (106), we get

$$\begin{aligned} x_0 &= \frac{\rho_0}{2\varepsilon} \\ \omega_1 &= \frac{2\varepsilon}{\rho_0^2} \sqrt{(4 - \rho_0^2)} \stackrel{\text{define}}{=} \omega_0 \end{aligned} \tag{107}$$

The rejection ratio ρ_0 at intersection point should satisfy $\rho_0 \in (0, 1)$. Moreover, due to $0 < \varepsilon \ll 1$, the selection of ρ_0 should make ω_0 bounded. Due to $2\sqrt{(4 - \rho_0^2)} > 1$ is bounded, we can select ρ_0 to make

$\frac{\varepsilon}{\rho_0} \leq 1$. Therefore, $\rho_0 \geq \varepsilon^{\frac{1}{2}}$ and $\rho_0 \in (0, 1)$ need to hold. We select $\rho_0 = \varepsilon^r \in (0, 1)$ (where, $r \in (0, \frac{1}{2}]$) to satisfy the above conditions. Then, at the intersection point, x_0 and ω_1 in (107) can be expressed respectively by

$$\begin{aligned} x_0 &= \frac{1}{2}\varepsilon^{r-1} \\ \omega_1 &= 4\varepsilon^{1-2r}\sqrt{1 - \frac{1}{4}\varepsilon^{2r}} \stackrel{\text{define}}{=} \omega_0 \end{aligned} \tag{108}$$

where, $r \in (0, \frac{1}{2}]$. For $\rho(\omega_1, x)$, when $x = x_0$ and $\omega_1 \geq \omega_0$, we get

$$\begin{aligned} \rho(\omega_1, x) &= \frac{1}{\sqrt{1 + \omega_1^2 x_0^2}} + \varepsilon \cdot x_0 \\ &\leq \frac{1}{\sqrt{1 + \omega_0^2 x_0^2}} + \varepsilon \cdot x_0 = \rho_0 \end{aligned} \tag{109}$$

Therefore, the error variable e_1 is in the bound:

$$\lim_{t \rightarrow \infty} |e_1| \leq \rho_0 L_1 \tag{110}$$

Due to $0 < \varepsilon \ll 1$ and $r \in (0, \frac{1}{2}]$, we can get $\rho_0 = \varepsilon^r \ll 1$. Also, the frequency $\omega_0 = 4\varepsilon^{1-2r}\sqrt{1 - \frac{1}{4}\varepsilon^{2r}}$ can be small enough. Thus, the disturbance $d_1(t)$ is rejected sufficiently in the frequency band $[\omega_0, \infty)$.

Determination of corrector parameter k_1

Because $k_1 = \frac{1}{x_0}$, the parameter k_1 is selected as

$$k_1 = \frac{1}{x_0} = 2\varepsilon^{1-r} \tag{111}$$

Rejection ratio for frequency band $\omega_1 \in [0, \infty)$

When the corrector parameter $k_1 = \frac{1}{x_0} = 2\varepsilon^{1-r}$ is selected, i.e. $x = x_0 = \frac{1}{2}\varepsilon^{r-1}$, the rejection ratio (99) is described by:

$$\rho(\omega_1) \stackrel{\text{define}}{=} \rho(\omega_1, x_0)|_{x=x_0} = \frac{1}{\sqrt{1 + \frac{1}{4}\varepsilon^{2r-2}\omega_1^2}} + \frac{1}{2}\varepsilon^r \tag{112}$$

We find that the rejection ratio $\rho(\omega_1)$ in (112) is a monotonically decreasing function of disturbance frequency $\omega_1 \in [0, \infty)$, and it satisfies:

- i) When $\omega_1 = \omega_0 = 4\varepsilon^{1-2r}\sqrt{1 - \frac{1}{4}\varepsilon^{2r}}$, we have $\rho(\omega_0) = \rho_0 = \varepsilon^r$; and $\rho(\omega_1) \rightarrow \frac{1}{2}\varepsilon^r$ as $\omega_1 \rightarrow \infty$. Therefore, in the frequency band $[\omega_0, \infty)$, $\rho(\omega_1) : \varepsilon^r \rightarrow \frac{1}{2}\varepsilon^r$ as $\omega_1 : \omega_0 \rightarrow \infty$.
- ii) When $\omega_1 = \omega_c = \frac{\varepsilon^{1-\frac{1}{2}r}\sqrt{4-\varepsilon^r}}{1-\frac{1}{2}\varepsilon^r}$, we have $\rho(\omega_c) = 1$. Therefore, in the frequency band (ω_c, ω_0) , $\rho(\omega_1) : 1 \rightarrow \varepsilon^r$ as $\omega_1 : \omega_c \rightarrow \omega_0$.
- iii) When $\omega_1 = 0$, we have $\rho(0) = 1 + \frac{1}{2}\varepsilon^r$; and $\rho(0) \approx 1$ due to $0 < \varepsilon \ll 1$ and $r \in (0, \frac{1}{2}]$. Therefore, in the frequency band $[0, \omega_c]$, $\rho(\omega_1) : 1 + \frac{1}{2}\varepsilon^r \rightarrow 1$ (or $\rho(\omega_1) \approx 1$) as $\omega_1 : 0 \rightarrow \omega_c$.

We know that $\omega_c = \frac{\varepsilon^{1-\frac{1}{2}r}\sqrt{4-\varepsilon^r}}{1-\frac{1}{2}\varepsilon^r} < \frac{\varepsilon^{1-\frac{1}{2}r}\sqrt{4}}{1-\frac{1}{2}} = 4\varepsilon^{1-\frac{1}{2}r} \ll 1$ because of $0 < \varepsilon \ll 1$ and $r \in (0, \frac{1}{2}]$. Therefore, the frequency band $[0, \omega_c]$ is sufficiently small. In general, the disturbance $d_1(t)$ in position measurement can be rejected sufficiently by the corrector even the the disturbance frequency covers the low/mid/high frequency bands.

This concludes the proof. ■

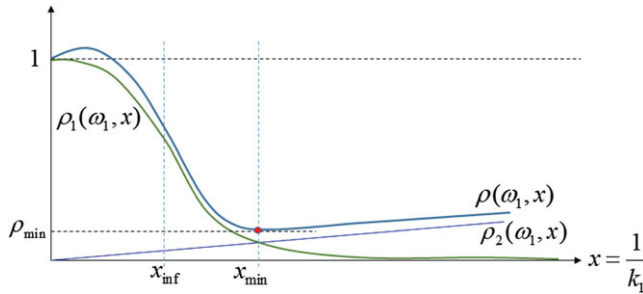


Figure 11. $\rho(\omega_1, x)$ curve and its minimum value.

Proof of Theorem 4.3

We know that the rejection ratio (99) is a monotonically decreasing function of frequency ω_1 . Therefore, in the given frequency band $[\omega_{req}, \infty)$, the rejection ratio satisfies

$$\rho(\omega_1, x) = \frac{1}{\sqrt{1 + \omega_1^2 x^2}} + \varepsilon \cdot x \leq \frac{1}{\sqrt{1 + \omega_{req}^2 x^2}} + \varepsilon \cdot x = \rho(\omega_{req}, x) \tag{113}$$

and

$$\lim_{t \rightarrow \infty} |e_1| \leq \rho(\omega_{req}, x)L_1 \tag{114}$$

In the following, we will determine x to get $\min \{ \rho(\omega_{req}, x) \}$. Taking the derivatives for $\rho(\omega_{req}, x)$ about x , we get

$$\frac{d\rho(\omega_{req}, x)}{dx} = -\omega_{req}^2 x (1 + \omega_{req}^2 x^2)^{-\frac{3}{2}} + \varepsilon \tag{115}$$

$$\frac{d^2\rho(\omega_{req}, x)}{dx^2} = 2\omega_{req}^4 (1 + \omega_{req}^2 x^2)^{-\frac{5}{2}} \left[x^2 - \frac{1}{2\omega_{req}^2} \right] \tag{116}$$

According to (115) and (116), $\rho(\omega_{req}, x)$ is the convex function about x when $x^2 < \frac{1}{2\omega_{req}^2}$, and $\rho(\omega_{req}, x)$ is the concave function about x when $x^2 > \frac{1}{2\omega_{req}^2}$. In order to get the minimum value of $\rho(\omega_{req}, x)$, the selection of x should make $\rho(\omega_{req}, x)$ about x be concave function, i.e. $\frac{d^2\rho(\omega_{req}, x)}{dx^2} > 0$ holds. Therefore, from (116), the following inequality should be satisfied:

$$x^2 > \frac{1}{2\omega_{req}^2} \tag{117}$$

Then, it follows that

$$x > \frac{1}{\sqrt{2}\omega_{req}} \stackrel{\text{define}}{=} x_{inf} \tag{118}$$

Therefore, $\rho(\omega_{req}, x)$ is the concave function in the range $x \in (x_{inf}, \infty)$, and x_{inf} is the curve inflection point (see Figure 11). From the concave property of $\rho(\omega_{req}, x)$ in the range $x \in (x_{inf}, \infty)$ and $0 < \varepsilon \ll 1$, the minimum value ρ_{min} of $\rho(\omega_{req}, x)$ exists when $\frac{d\rho(\omega_{req}, x)}{dx} = 0$, i.e.

$$\frac{d\rho(\omega_{req}, x)}{dx} = -\omega_{req}^2 x (1 + \omega_{req}^2 x^2)^{-\frac{3}{2}} + \varepsilon = 0 \tag{119}$$

Define the solution to (119) in $x \in (x_{\text{inf}}, \infty)$ is x_{min} . Then, the minimum value ρ_{min} of $\rho(\omega_{\text{req}}, x)$ can be expressed by

$$\rho_{\text{min}} \stackrel{\text{define}}{=} \min \{ \rho(\omega_{\text{req}}, x) \} = \frac{1}{\sqrt{1 + \omega_{\text{req}}^2 x_{\text{min}}^2}} + \varepsilon \cdot x_{\text{min}} \quad (120)$$

It means that, when we select the corrector parametre $k_1 = 1/x_{\text{min}}$, and x_{min} is the solution to (119) in the range $x \in (x_{\text{inf}}, \infty)$, the rejection ratio can be expressed by

$$\rho(\omega_1) \stackrel{\text{define}}{=} \rho(\omega_1, x)|_{x=x_{\text{min}}} = \frac{1}{\sqrt{1 + x_{\text{min}}^2 \omega_1^2}} + \varepsilon \cdot x_{\text{min}} \quad (121)$$

The rejection ratio $\rho(\omega_1)$ is a monotonically decreasing function of disturbance frequency ω_1 , and it satisfies:

- i) In $[\omega_{\text{req}}, \infty)$, $\rho(\omega_1) : \rho_{\text{min}} \rightarrow \varepsilon \cdot x_{\text{min}}$ as $\omega_1 : \omega_{\text{req}} \rightarrow \infty$.
- ii) In $(\omega_c, \omega_{\text{req}})$, $\rho(\omega_1) : 1 \rightarrow \rho_{\text{min}}$ as $\omega_1 : \omega_c \rightarrow \omega_{\text{req}}$, where, $\omega_c = \frac{\sqrt{\frac{2\varepsilon}{x_{\text{min}}}} \sqrt{1 - \frac{1}{2} \varepsilon x_{\text{min}}}}{1 - \varepsilon \cdot x_{\text{min}}}$.
- iii) In $[0, \omega_c]$, $\rho(\omega_1) : 1 + \varepsilon \cdot x_{\text{min}} \rightarrow 1$ as $\omega_1 : 0 \rightarrow \omega_c$.

Therefore, the disturbance $d_1(t)$ in the frequency band $[\omega_{\text{req}}, \infty)$ is rejected sufficiently. This concludes the proof. ■

Proof of Theorem 5.1

Define $e_1 = x_1 - p_0(t)$, and $e_2 = x_2 - v_0(t)$. Then, the system error can be expressed by

$$\begin{aligned} \dot{e}_1 &= e_2 \\ \dot{e}_2 &= \begin{cases} -k_3 \text{sign}[e_2 - d_2(t)] - \dot{v}_0(t), & \text{if } |e_2 - d_2(t)| > 1; \\ -k_2 \text{sign}[e_2 - d_2(t) + k_1(e_1 - d_1(t))] - \dot{v}_0(t), & \\ 1r & \text{if } |e_2 - d_2(t)| \leq 1 \end{cases} \end{aligned} \quad (122)$$

Define $d_3(t) = d_4(t) = \dot{v}_0(t)$, the system error (122) is rewritten as

$$\begin{aligned} \dot{e}_1 &= e_2 \\ \dot{e}_2 &= \begin{cases} -k_3 \text{sign}(e_2 - d_2(t) - d_3(t)), & \text{if } |e_2 - d_2(t)| > 1; \\ -k_2 \text{sign}[e_2 - d_2(t) + k_1(e_1 - d_1(t))] - d_4(t), & \\ 1r & \text{if } |e_2 - d_2(t)| \leq 1 \end{cases} \end{aligned} \quad (123)$$

According to Theorem 4.2, we can get the bounds of the estimate errors (18) and the other conclusions. This concludes the proof. ■